RICE UNIVERSITY

Transport Phenomena In Molecular-Scale Devices

by

Zachary Keane

A Thesis Submitted
in Partial Fulfillment of the
Requirements for the Degree

Doctor of Philosophy

Approved, Thesis Committee:

_____

Douglas Natelson, Chair
Associate Professor of Physics and
Astronomy
Associate Professor of Electrical and
Computer Engineering

_____

Emilia Morosan
Assistant Professor of Physics and
Astronomy

_____

Kevin Kelly
Associate Professor of Electrical and
Computer Engineering

Houston, Texas

September, 2009

ABSTRACT

Transport Phenomena In Molecular-Scale Devices

by

Zachary Keane

The physics of atomic-scale systems is a subject of considerable interest, from both a basic-science and an engineering standpoint. We discuss three sets of experiments, each designed to elucidate a particular aspect of nanoscale physics. The first of these aspects is spin-dependent transport in atomic-scale ferromagnetic wires. Early reports of large magnetoresistive effects in this type of device led to speculation about possible mechanisms for enhancing spin polarization in ferromagnetic constrictions, as well as excitement about the potential applications for such an effect. An experiment carefully designed to exclude other mechanisms for conductance changes, however, leads us to conclude that there is no evidence for a large magnetoresistive effect *per se* in constricted ferromagnetic wires.

A second area of interest is hysteretic conductance switching in single-molecule transistors incorporating bipyridyl dinitro oligo(phenylene ethynylene) dithiol (BPDN-DT). An early hypothesis to explain the observed hysteresis involved strong electron-vibration coupling leading to shifts in molecular energy levels. A change in the charge state of the molecule could both lead to a change in the conductance across the molecule and tend to stabilize the charge on the molecule, leading to hysteretic switching behavior. To examine this hypothesis, we fabricated and measured three-terminal devices allowing us to control the charge on the molecule independent of the

source-drain bias. We find that the evidence argues against a charge-transfer-based mechanism for the conductance switching; instead, it is more likely that a change in the molecule-electrode coupling is responsible for this behavior.

The final area addressed in this dissertation is that of current-dependent electronic noise in single molecules. In many nanoscale devices, the discrete nature of the carriers of electric current leads to fluctuations about the average current; these fluctuations are known as shot noise. Correlations between the charge carriers can change the dependence of the magnitude of this shot noise on the value of the average current. One of the best-known examples of a correlated-electron effect in single-molecule conductance is the Kondo effect. Theorists have predicted that a single-molecule transistor in the Kondo state would exhibit significantly enhanced shot noise. We discuss the experimental challenges in making single molecule noise measurements, as well as possible techniques to address these challenges.

Acknowledgments

I owe my gratitude to a number of people, without whose help this work would not have been possible. To begin with, I want to thank my advisor, Doug Natelson. I have a great deal of admiration for his impressive knowledge of physics, but that is far from the most important aspect of our working relationship. He has been a source of advice when I have needed it, encouragement when I have hit the occasional slump, and forbearance when I have made the occasional laboratory blunder. Without his aid, this work would have been quite literally unthinkable.

I am also grateful to my other two committee members, Emilia Morosan and Kevin Kelly, for taking the time and putting forth the effort to read and comment on this monstrous document. I know it can't have been easy.

To Lam Yu, Aaron Trionfi, Behrang Hamadani, and Jay Lee, the senior students when I joined the Natelson group: Thank you for taking the time to teach me so much of what you know. Training in electron microscopy and e-beam lithography is probably the smallest way in which I benefited from your experience and wisdom. Each of you has nudged me in the right direction from time to time when I have tended to flub a measurement or a fabrication step, and I deeply appreciate your often-extraordinary patience.

To Dan Ward, Jeff Worne, Patrick Wheeler, Alexandra Fursina, Kenny Evans, and Amanda Whaley: You are the future of the Natelson group, and the future is bright. I have often benefited from being able to run ideas by you, and I would even venture to say that I've learned a thing or two from our various discussions. It goes without saying that the last several years would not have been the same without you — thank you for keeping things interesting.

I owe special thanks to the chemists in the Tour group, particularly Jake Ciszek. Without their expertise in organic synthesis and their willingness to share the product of their labors, none of our work on single-molecule devices would have been possible.

Thanks go to Alex Rimberg and Tim Gilheart for advice and technical assistance related to the design and implementation of the voltage amplifiers needed to carry out the single-molecule noise measurements.

Without the staggering array of incredibly talented teachers who have guided me in some way over my years of schooling, it is certain that I would not be where I am today. Though there are too many to name, I am sincerely grateful for their patience and assistance at each stage of my education.

Finally, I owe a great deal to my family, without whose love and support I could never have come as far as I have, and to my Valhalla family, without whom I could never have retained my sanity through the journey. Thank you for all you have done, and I hope I can continue to make you proud.

Contents

Illustrations

Tables

Chapter 1

Introduction

1.1 Preface

This thesis covers a fair amount of ground, ranging from magnetotransport proper-
ties of purely metallic devices through switching behavior in single molecules to the
electronic noise in molecular-scale devices. The overarching theme here is that each
of these systems is physically very small, and therefore may be expected to have
properties somewhat different from bulk systems. Anyone reading this will undoubt-
edly be familiar with Feynman's 1959 observation that "there's plenty of room at
the bottom" — that is, that it would be possible, for quite some time, to simply
miniaturize existing devices and go forward in that manner — but the more relevant
observation to this thesis is that "small is different." It is well established, for ex-
ample, that semiconductor quantum dots with sizes from 2-50 nm exhibit an array
of interesting properties [1]. Quantum confinement in CdSe nanocrystals yields a
tunable bandgap and the attendant optical properties, while the high surface area to
mass ratio of magnetite nanocrystals may be used to further the removal of arsenic
from groundwater [2].

Of course, the quantum effects inherent in nanoscale systems do not always inure

to our benefit. Moore's law posits that the number of transistors on a chip will double roughly every 12-24 months, but it is becoming increasingly clear that blindly scaling silicon CMOS technology will not continue to work forever. Quantum tunneling across gate oxides, for example, is rapidly increasing power dissipation as gate lengths get smaller [3], and while work is underway to address this and several other issues inherent in scaling down CMOS architecture [4], bulk semiconductors will not be able to continue to provide the scaling needed to continue Moore's law. It is therefore of considerable interest to examine other modalities for providing functionality at these length scales. A single-molecule transistor consisting of a small organic molecule coupled to source, drain, and gate electrodes could be said to represent the ultimate limit of scaling for the field-effect transistor, as the channel length would be on the order of a few nm. While the fabrication challenges inherent in making devices at this scale, most notably the low ($\sim 10\%$) yield, render it unlikely that integrated circuits will ever incorporate large numbers of single-molecule elements, these types of devices can nevertheless serve as a useful testbed both for evaluating the properties of different molecules and for exploring the physics behind electron transport at this scale.

One way of examining the electronic properties of nanoscale systems is to look at their conduction — by applying a voltage and looking at the current produced, we can infer a lot about the underlying processes. It is possible in principle to simulate nanoscale systems in exacting detail, solving the full nonequilibrium quantum

mechanics to determine what the conduction should be under different conditions, but this is wildly impractical given the scale of the problem. Instead, a number of models have been developed that produce particular behaviors relevant to different situations. Chapters 2 and 3 of this thesis detail experiments relevant to two of these models.

1.2 Transport through one-dimensional wires

In Chapter 2, we examine the electronic transport properties of a ferromagnetic wire linking two bulk contacts. As the wire is progressively constricted to a few-atom contact, features appear in the conduction that cannot be explained in terms of the bulk resistivity and the cross-sectional area. Instead, as the transverse width of the system approaches the effective wavelength of the electrons, transport takes place through a small number of quantum channels — the conductance becomes quantized. The Landauer-Büttiker formalism, illustrated in Fig. 1.1, is a useful model in this instance, as the wire becomes, effectively, a one-dimensional conductor coupled to two large reservoirs. While this model neglects spin-dependent transport effects and any correlations between the charge carriers, it does a reasonably good job of explaining the transport through constricted wires. In addition, since the Landauer-Büttiker model treats the spin-up and spin-down current separately, it is relatively straightforward to extend it to include certain spin-dependent effects.

To understand the Landauer-Büttiker model, consider exactly the case described
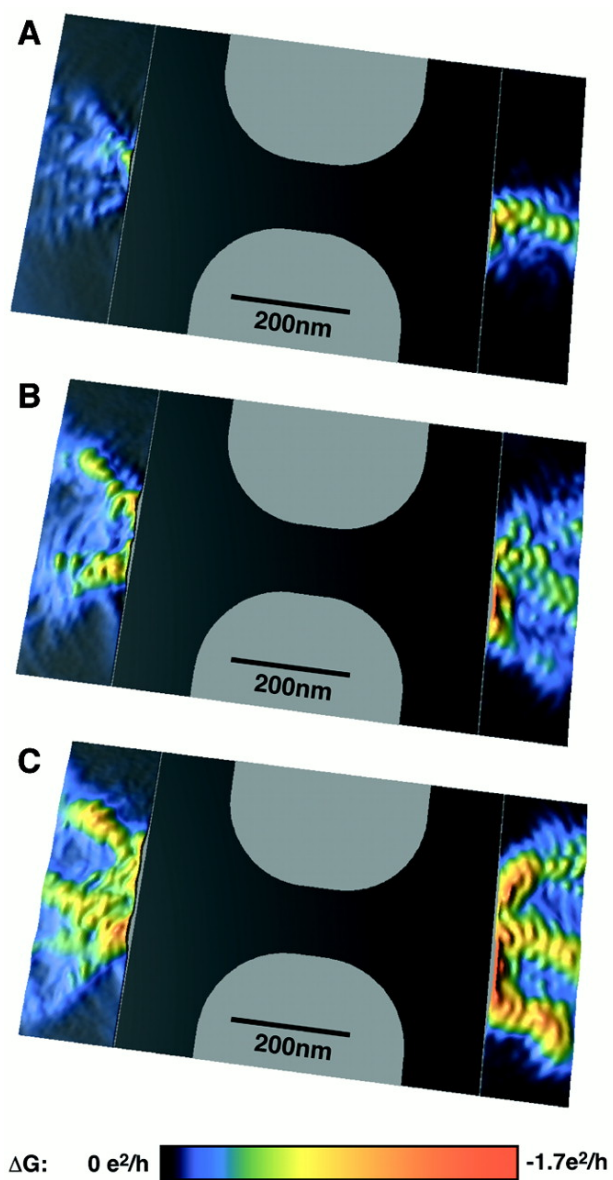
Figure 1.1 : (Adapted from [5]) Images of coherent electron flow in a quantum point contact with one, two, and three channels open. The Landauer-Büttiker formalism describes this type of transport well.

above, of a one-dimensional wire coupled to two large reservoirs of charge at $T = 0$ with chemical potentials μ_L and μ_R. Then the voltage difference ΔV between the two reservoirs is $e(\mu_L - \mu_R)$. In the case where $\Delta V > 0$, occupied states move from reservoir 1 to reservoir 2 along the wire, leading to a current

$$j = (-e)(\mu_L - \mu_R)(v\frac{dn}{d\mu}) \tag{1.1}$$

where e is the electric charge, v is the Fermi velocity in the tube, and $\frac{dn}{d\mu}$ is the density of states at the Fermi surface. Since there are two independent spin species, the density of states $\frac{dn}{d\mu} = \frac{2}{hv}$. Given this, we obtain the following expression for the conductance of a perfectly-transmitting one-dimensional wire:

$$G = \frac{j}{\Delta V} = \frac{2e^2}{h}. \tag{1.2}$$

This expression can be extended in a straightforward manner to account for the possibility of multiple conducting channels and for transmission coefficients less than 1. Specifically, for a system with n channels, each with transmission coefficient T_i, we obtain

$$G = \sum_{i=1}^{n}(T_i\frac{2e^2}{h}). \tag{1.3}$$

There is significant experimental support for this model in various physical implementations, including semiconductor quantum point contacts and constricted metallic wires.

1.3 Transport through a single molecule

Chapter 3 deals with the transport through a molecule sandwiched between a pair of bulk leads. In many cases, such molecules are relatively weakly bound to the leads, and so the electronic states are well-localized on the molecule. In a single-molecule system, the small size of the molecule and the large spacing between molecular energy levels virtually ensure that the level spacing is much larger than the thermal energy kT. In these cases, it makes sense to think of the molecule as having a discrete energy spectrum, and the system is well-approximated as a quantum dot coupled to each lead by an effective tunneling barrier. While the double-barrier problem has been extensively studied in semiconductor quantum dots and metallic single-electron transistors, there are significant differences between the single-molecule case and the semiconductor case. First, the energy scales are different by several orders of magnitude: while the level spacing in semiconductor quantum dots may be measured in microvolts, and that in metallic SETs may be nanovolts, typical energy scales for molecules are generally in the hundreds of millivolts to over 1 V. This enables operation of single-molecule devices at relatively high temperatures — a simple helium-4 cryostat can easily bring kT well below the relevant energy scales. Second, the hierarchy of energy scales is reversed in single-molecule devices as compared to solid-state SETs: molecular electronic levels are generally widely spaced compared to the vibrational modes, while semiconductor electronic levels are closely spaced, with vibrational energy scales farther apart.

Much of the physics familiar from solid-state double-barrier structures remains in the molecular case, though. In particular, Coulomb blockade is as important in single-molecule devices as it is in semiconductor SETs. Coulomb blockade arises when there is a mismatch between the energy levels of filled electronic states on the leads and empty states on the quantum dot. Since the dot has a discrete set of energy states, and the ones below the Fermi level of the leads are generally full, tunneling onto the dot is inhibited at low source-drain bias. Once the Fermi level of the source electrode is brought into alignment with an empty state on the dot, electrons can tunnel onto the empty state and out into the drain electrode, a process known as resonant transport. This is manifested as a series of steps in the $I-V$ curve of the quantum dot, or a series of peaks in the differential conductance $\frac{dI}{dV}$. Of course, higher-order processes can and do contribute to conduction away from energetic resonances. In these cases, an electron can tunnel onto a classically forbidden state and out into the electrode.

Generally the contribution of off-resonant tunneling is small compared to the resonant tunneling processes, but there are exceptions. One such exception is a correlated-electron process known as the Kondo effect (see Figure 1.2). The Kondo effect arises when there is an unpaired electron on a quantum dot below the Fermi energies of the source and drain electrodes. This can occur, for example, when a molecular energy state is nominally below the Fermi energy of the bulk, but the on-site repulsion prevents the state from being doubly occupied. In this scenario, an electron with spin opposite that of the unpaired electron on the dot can tunnel onto

the dot as the electron on the dot moves off. This provides a pathway for enhanced

conduction, and is manifested as a peak in the differential conductance across the dot

at low temperatures and near zero bias.
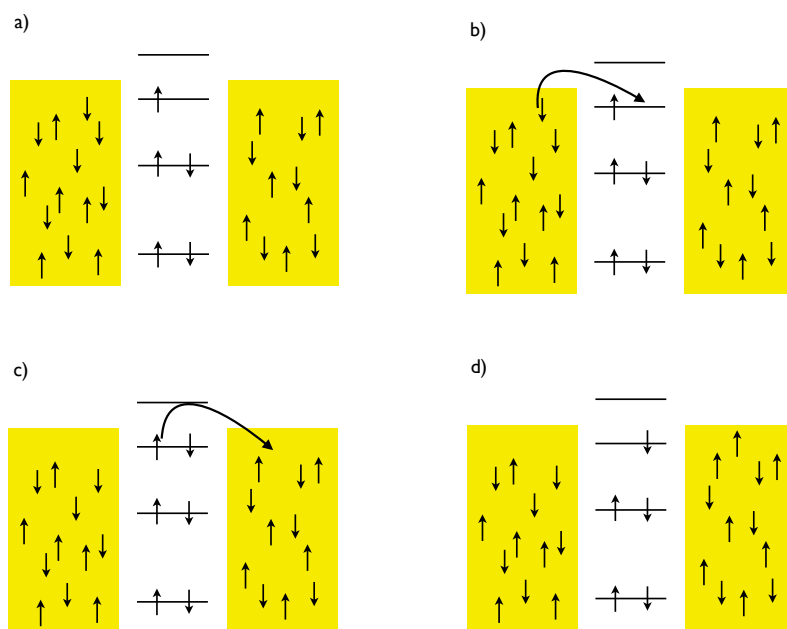
Figure 1.2 : Graphical representation of the mechanism for Kondo-mediated conduction enhancement. (a) Initial state; on-site Coulomb repulsion prevents charge transfer between molecule and electrode. (b) — (c) Formation and resolution of the classically forbidden Kondo state. (d) Final state; note the change in the spin remaining on the molecule.

1.4 Electronic correlations and noise

While DC conductance measurements can elucidate much of the physics underlying electron transport in nanoscale structures, they do not by any means tell us everything. For example, imagine having a complete, ordered list of the times when electrons transited a particular device. One in possession of such a list could compute much more than just the average current — also available would be the fluctuations about the average current, as well as higher-order statistical moments. Conversely, a direct measurement of these higher statistical moments can shed some light on the characteristics of the ordered list of arrival times. A measurement of shot noise, for example, gives the fluctuations about the average current in a device. It may be that the electrons tend to arrive in bunches — this would yield large fluctuations in the current and therefore a large amount of noise. It may also be that the electrons have a tendency to arrive as evenly spaced as possible, in which case there would be very little noise indeed. Chapter 4 is a discussion of an experimental method for measuring shot noise in single molecules, as well as the experimental challenges of trying to implement this method.

Chapter 2

Magnetoresistance in Atomic-scale Electromigrated Nickel Nanocontacts

Magnetoresistive effects in ferromagnetic structures are of considerable technological and scientific interest. Read heads for magnetic storage media have evolved considerably over the past decade, particularly as a result of the discovery of giant magnetoresistance (GMR) [6]. Earlier magnetic read heads were based on anisotropic magnetoresistance in a ferromagnetic layer, which yields about a 2-3 percent change in resistivity [7]. GMR is a much larger effect, up to about 80 percent; this allowed much more sensitive magnetic detectors and higher data density. In the early 2000s, there were claims of a still larger effect, called ballistic magnetoresistance [8], which occured in atomic-scale constrictions in ferromagnetic wires. The goal of this experiment was to leverage our expertise in the fabrication of thin films and narrow constrictions to test some of these claims in a well-controlled environment.

The anisotropic magnetoresistance (AMR) results from spin-orbit scattering and is manifested as a change in resistivity, ρ, as a function of the relative orientation of the magnetization $\mathbf{M}$ and the current density $\mathbf{J}$ [9]. In Ni, for example, $(\rho(J \parallel M) - \rho(J \perp M))/\rho(J \parallel M) \approx 0.02$ [7]. In a randomly-magnetized bulk sample of material, then, the average resistivity $\rho_a v = \frac{2}{3}\rho(J \perp M) + \frac{1}{3}\rho(J \parallel M)$.

As stated above, AMR results from the spin-orbit interaction in d electrons in the lattice, and more specifically from the scattering of the s electrons responsible for the conductance from the stationary d electrons. It has been shown [10] that the probability of mixing between s and d states is smallest when the s electron is moving perpendicular to the plane of the d orbital lobes; accordingly, in all ferromagnetic transition metals the resistivity is at a minimum when the magnetization is perpendicular to the current density(see Fig. 2.1. Typically this effect results in a resistivity change of a few percent at room temperature.
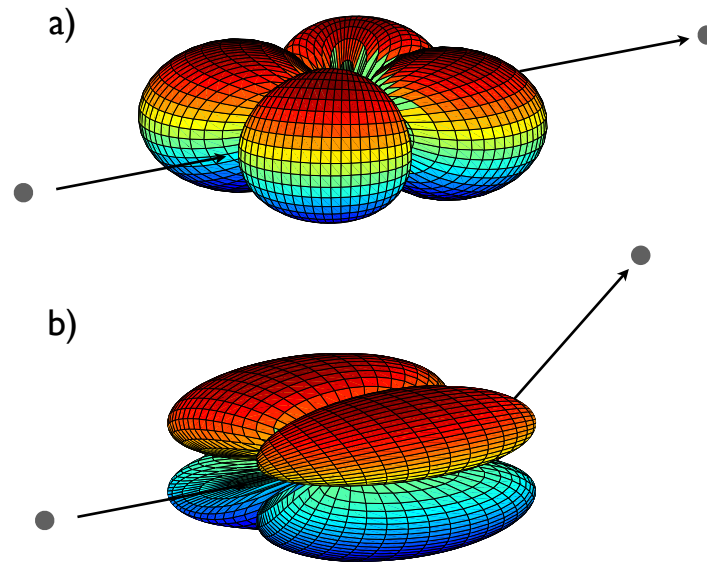
Figure 2.1 : Graphical representation of the mechanism for AMR. (a) $M \perp J$; resistance is at a minimum. (b) $M \parallel J$; resistance is maximized.

Tunneling magnetoresistance (TMR) results from the difference in majority and

minority densities of states at the Fermi level. Tunneling resistance, R, is generally
enhanced for antialigned magnetizations of the electrodes on either side of the tunnel
barrier(see Fig. 2.2). The magnitude of TMR in large area junctions is $\equiv (R_{\uparrow\downarrow} - R_{\uparrow\uparrow})/R_{\uparrow\uparrow} = 2P^2/(1 - P^2)$, where P is the spin polarization at the Fermi level [11].
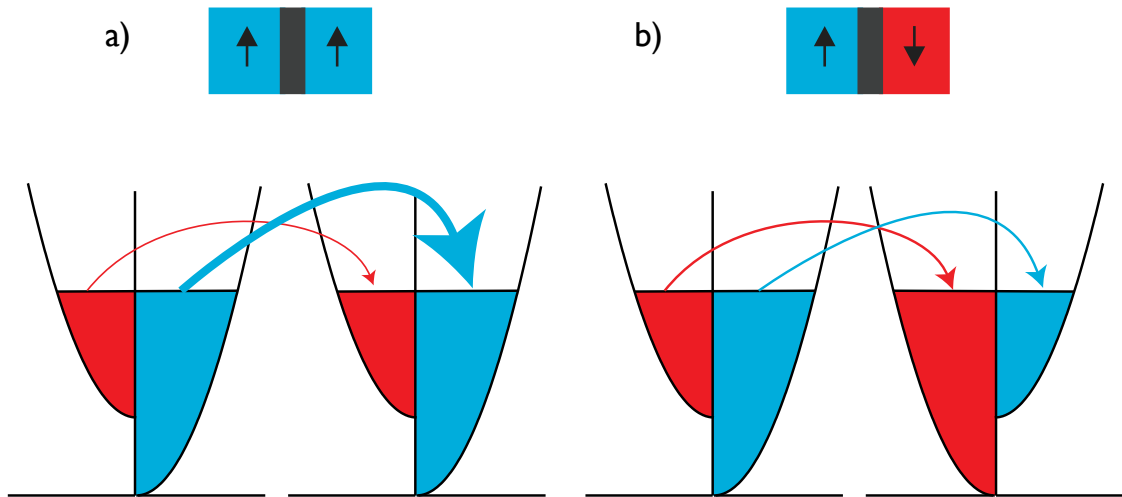
Figure 2.2 : Graphical representation of the mechanism for tunneling magnetoresistance. (a) Leads have parallel magnetization. Majority carriers tunnel into majority states; conduction is unaffected. (b) Leads have antiparallel magnetization. Majority carriers tunnel into minority states; conduction is suppressed.

The magnetoresistance of atomic-scale constrictions in magnetic wires has been
the subject of intense interest since the initial report of large ballistic magnetoresistance (BMR) in junctions between Ni wires [12]. BMR magnitudes reported in the
literature have ranged to in excess of 100,000 % [13]. These reports of BMR magnitudes far in excess of typical AMR and TMR effects have generated considerable
controversy, including concerns about magnetostrictive artifacts [14]. It is therefore of

interest to examine constrictions fabricated in a geometry that minimizes these effects and allows temperature-dependent studies of junction magnetoresistances. Previous experiments along these lines have used mechanical break junctions [15], planar electrochemically grown junctions [16], ballistic nanopores [17], and ion-beam-formed constrictions [18]

We have made measurements of the magnetoresistance through few-atom and single-atom contacts between planar Ni electrodes, as well as planar Ni-Ni tunnel junctions. Junctions are fabricated by a combination of electron beam lithography and controlled electromigration. This allows the examination of individual nanostructures with junction configurations serially modified from planar films to few-atom contacts to vacuum tunnel junctions. These planar structures are chosen to minimize magnetostrictive effects, as discussed below. Small junction size is confirmed by evidence of conductance quantization and discrete switching. At 10 K, conventional AMR is observed in large junctions, and increases in magnitude as the number of channels approaches one. We observe significant sample-to-sample variation in the shape and sign of the magnetoresistance, with an upper limit on the magnitude consistent with TMR in Ni of known properties. This variability, typical of mesoscopic systems, suggests that the bulk magnetization of the electrodes is not simply related to the local magnetization of the few atoms directly relevant for tunneling.

Devices are fabricated by a two-step lithography process on test grade $p+$ Si wafers coated with 200 nm thermal oxide. Ni structures are defined by e-beam lithography
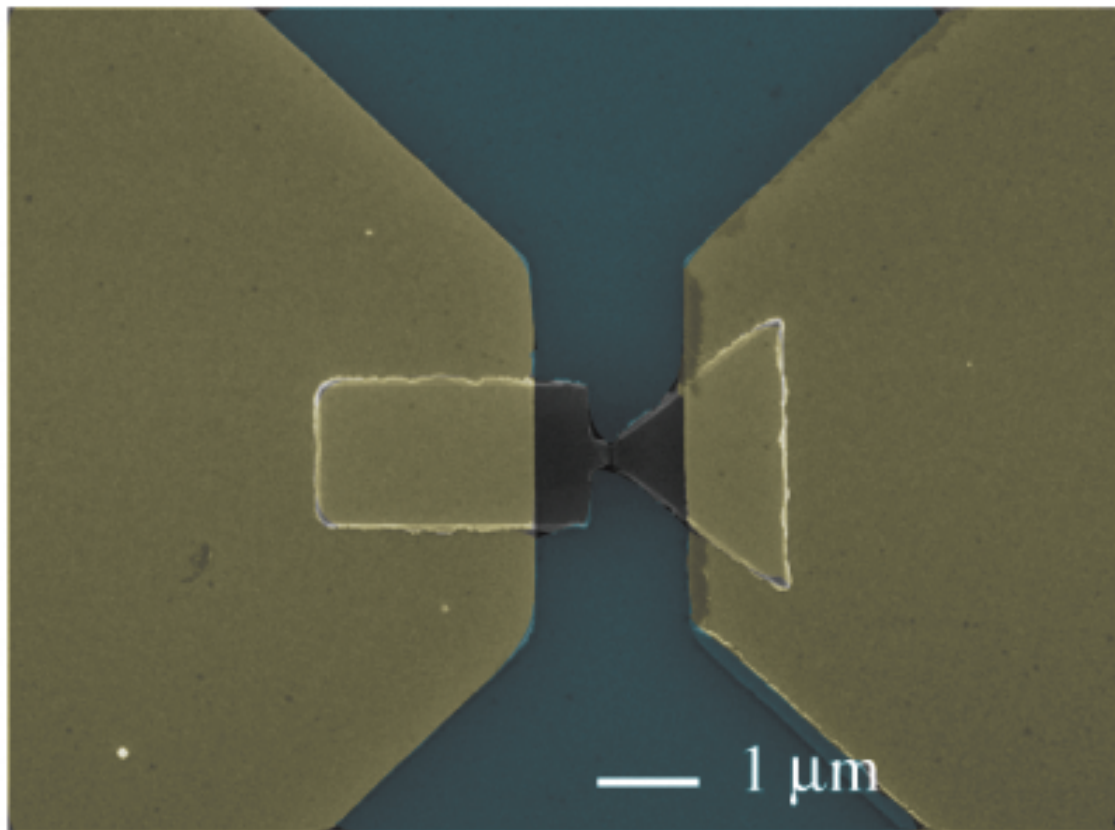
Figure 2.3 : Scanning electron micrograph of a typical device for magnetoresistance measurements. Leads are 1 nm Ti/30 nm Au; constricted wire is 20 nm thick Ni.

and e-beam evaporation (20 nm thick Ni film deposited at 2 Å/s in a system with $\sim 10^{-7}$ mB base pressure). This is followed by a second lithography step, Ar ion sputter cleaning to ensure good contact to the Ni layer, and evaporation of 1 nm Ti/30 nm Au leads to make electrical contact (see Appendix A for detailed fabrication recipes).

Sample geometries, shown in Fig. 2.3, were chosen to minimize magnetostrictive effects by anchoring the bulk electrodes firmly to the substrate, and to create a well-defined domain structure near the constriction so that the data could be more easily interpreted. The micron scale of the Ni pads increases the likelihood that each will consist of a single domain. The electrode shapes favor controlled relative reorientation of their bulk magnetizations [19, 20]. In the absence of an external magnetic field, $\mathbf{M}$ is favored to lie in the plane of the electrodes and parallel to the current.

The Ni constrictions are progressively broken by electromigration [21] to achieve contacts ranging from a few atoms to vacuum tunnel junctions. All measurements are performed at 10 K in a variable temperature vacuum cryostat to mitigate oxidation of the Ni atoms near the contact. The system is relatively stable at this temperature, allowing measurement of the same device in multiple configurations; in this way we were able to observe the evolution of these devices from bulk metal through the ballistic regime into the tunneling regime.

To achieve few-atom contacts and clean vacuum tunnel junctions reliably, precise control of the electromigration procedure is paramount; our procedure for nickel
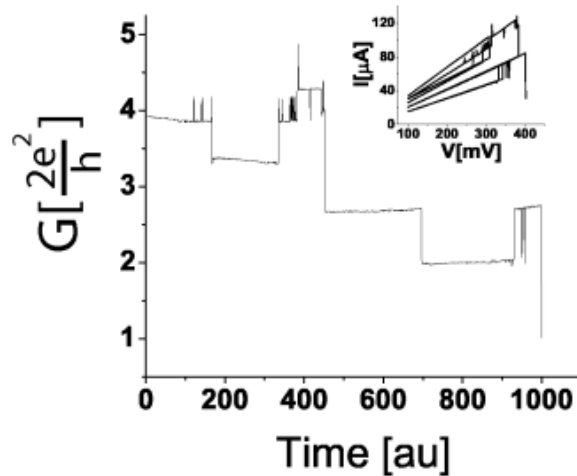
Figure 2.4 : Conductance vs. time for a successful electromigration run, demonstrating discontinuities and conductance plateaux. Total duration of the data shown is approximately 10 seconds. (inset) $I - V$ curves representing the same data.

closely follows one previously reported for room-temperature gold nanojunctions [22]. The electromigration process is carried out under computer control by means of a LabVIEW-based control program, a National Instruments analog input/output board, and a Stanford Research Systems current amplifier. Typical measured starting resistances are on the order of 80-100Ω; this figure includes both the device itself and the resistance of the cabling. The process entails an initial I-V measurement at low voltages to determine the device's starting resistance; next, the voltage is swept upward and the current monitored until the device's resistance has reached an upper bound calculated from the starting resistance. This indicates that the contact has begun to break, and at this time the current is stopped to avoid catastrophic failure. The process then repeats with the new baseline resistance until the desired final resistance is reached.

Achieving stable few-channel junctions is extremely challenging, with a success rate of $\sim 8\%$. Current-voltage curves and corresponding conductance data from a successful electromigration run resulting in a 13 kΩ device are shown in Fig. 2.4. The discontinuities in the last few $I - V$ curves, and the corresponding conductance plateaux, indicate that the device under test likely consists of a few atoms at its narrowest point. Such few-channel junctions often exhibit telegraph noise with conductance changes $\sim e^2/h$, also consistent with extremely narrow constrictions.

After the electromigration procedure reaches the desired endpoint (often a few kΩ, a value consistent with a few-atom contact), the magnetoresistance is measured with lock-in amplifier techniques. For high-conductance devices, the differential resistance measurement is performed by sourcing a current of up to 100 μA at a frequency near 1 kHz and monitoring the voltage across a device as the magnetic field is varied. For devices in the tunneling regime (generally > 100kΩ), by contrast, it is more convenient to source a voltage (generally no more than a few mV) at a lower frequency (10-200 Hz, depending on the conductance) and measure the resulting current.

A family of magnetoresistance curves from one electromigrated device is shown in Fig. 2.5. The magnetization of the leads lies in the plane of the film until a coercive external field is applied out of plane. An *in situ* rotation stage allows the acquisition of magnetoresistance data as a function of field orientation for a single junction configuration. The magnetoresistance under a transverse field evolves gradually from a small AMR in the bulk to a larger, similarly-shaped curve as the device is broken into

Table 2.1 : Magnetoresistance of samples under various electromigrated configurations.

Sample	Resistance	Longitudinal MR [%]	Transverse MR [%]
A	7.1 kΩ	0.78	1.14
A	83 kΩ	20.7	16.4
B	13 kΩ	20.5	8.03
B	5 MΩ	11.3	10.7
C	10 MΩ	9.43	7.07
D	13 kΩ	5.13	10.7
D	200 kΩ	13.3	[not measured]
E	5.8 kΩ	3.3	15.4
E	13 kΩ	8.69	21.9

the ballistic regime. The initial magnitude of the out-of-plane MR in an unbroken starting device is typically a few tenths of a percent; while AMR in nickel films is typically 2%, the smaller value is reasonable since initially the measured resistance is dominated by the leads and wiring.

As the device is progressively broken, the MR quickly approaches and then surpasses the expected magnitude for bulk AMR: in few- and single-channel devices, this effect can approach 20%. Finally, in the tunneling regime, we see fairly typical MR magnitudes for a vacuum tunnel junction, with TMR values of 10-20%. Table 2.1 shows several samples measured in different electromigrated configurations at 10 K.

A closer look at the curves in Fig. 2.5 reveals some aspects, other than the surprisingly large magnitude of the AMR-like effect, in which the behavior of these devices diverges from traditional AMR. The most readily apparent of these unusual behaviors is the appearance of switching features at applied fields of around 2 kOe perpendicular to the current. These features are not observed in any devices prior to electromigration. The hysteretic nature of these switching features suggests that they may be due to domain reversal in the Ni metal. In both in-plane and out-of-plane field sweeps, the magnitude and sign of the TMR has significant variability from device to device. While there are suggestions in the literature of a ballistic variant of AMR [23], these predictions call for the abrupt opening or closing of a full conductance channel, an effect not seen in these devices.

Given the controversy surrounding claims of large ballistic magnetoresistance, it was important to separate the behavior intrinsic to the metallic contact from possible confounding effects. Magnetostriction is one such effect: one need only cause a single- atom mechanical contact to shift by a fraction of a nanometer to cause a large conductance change. One experiment designed to quantify the effects of magnetostriction in nickel mechanical break junctions indicates that, in a geometry with a 650 nm undercut beneath the bridge, magnetostriction accounted for a 40% change in the resistance of an atomic-scale contact [24]. Since the magnetoresistance values measured in our experiment are of the same order, this was a cause for some concern.

In the end, we have found that magnetostriction is very unlikely to account for
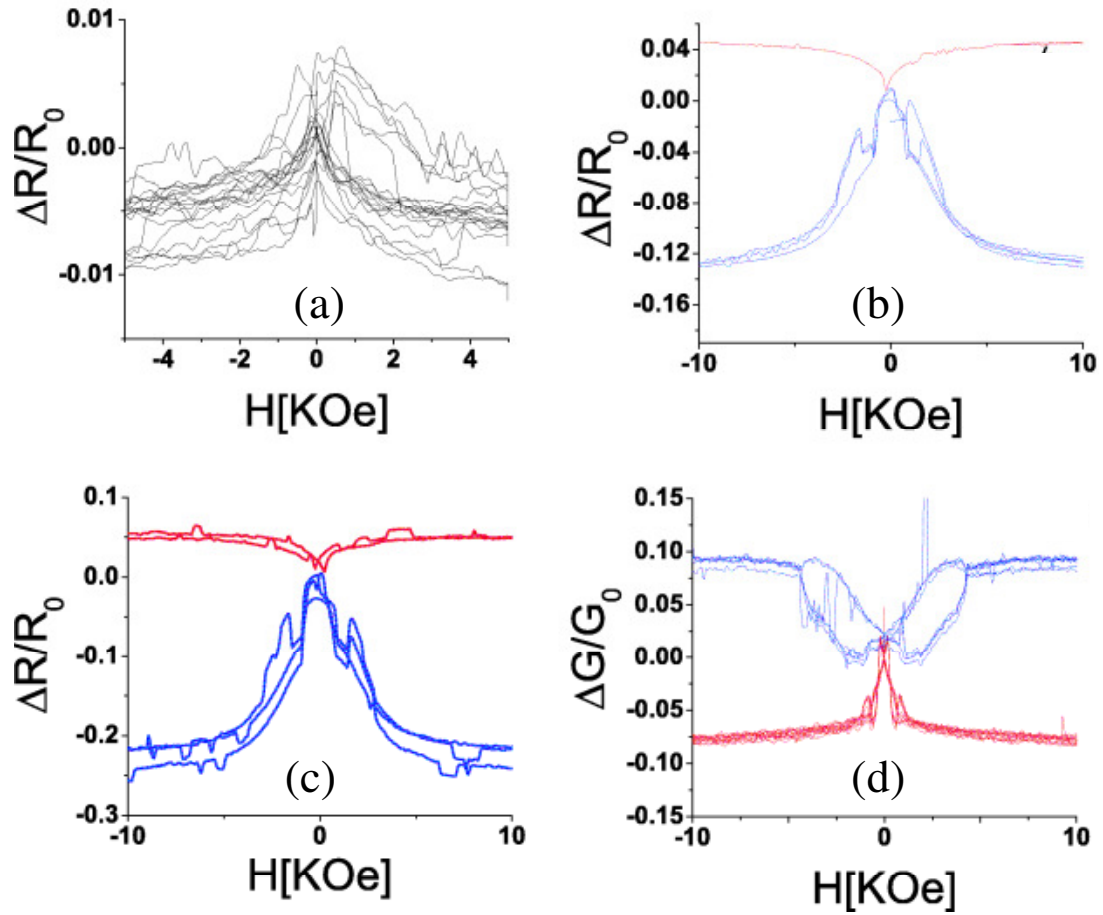
Figure 2.5 : a) Anisotropic magnetoresistance of a typical device (sample E) before electromigration. b) In-plane (upper) and out-of-plane (lower) magnetoresistance of sample E at 5.8 kΩ. c) In-plane (upper) and out-of-plane (lower) magnetoresistance of sample E further broken to 13 kΩ. d) In-plane (lower) and out-of-plane (upper) magnetoconductance of a 10 MΩ tunnel junction (sample C).

these results for two reasons. First, in our geometry, the Ni wires are constrained by the silicon substrate everywhere except for the immediate neighborhood of the constriction; the length of the bridge which is unconstrained by the substrate below is at most ~10 nm, which should result in a much smaller magnetostrictive effect. Second, the magnetoresistance curves shown in [24] are qualitatively different from those reported here, particularly in the lack of fine structure.

The complicated MR patterns and variability indicate that domain structure in the bulk electrodes is not simply related to the atomic-scale magnetization at few-atom contact or point of tunneling. Since there is no evidence of Coulomb blockade as these devices approach the TMR limit, it is unlikely that the effects seen are a result of unintentional nanoparticle formation during electromigration. Similar variability and complicated magnetic structure has also been seen in mechanical break junction experiments in the few-channel regime [15]. Such strong sensitivity to detailed contact geometry has also been supported theoretically [25].

Three factors are likely to be relevant to understanding these observations. First, single-molecule transistor measurements with ferromagnetic leads [20] have explicitly demonstrated that effective exchange fields at surface atoms can be large (70 T) and different from the bulk. Second, tunneling via localized states (possibly surface states in this case) has been demonstrated to lead to inverted TMR [26], as have highly transmitting channels [27]. Third, it is possible that trace amounts of NiO_x or unintended adsorbates at the tunneling point can cause local perturbations of the

tunneling spins. Detailed atomic-scale variations in the junctions clearly can have a profound influence on relevant magnetoresistive processes.

It is of interest that a group at Cornell independently pursued a directly analogous project, using permalloy films in place of nickel [28]. Their findings essentially replicate those presented here, lending further support to the contention that large values of ballistic magnetoresistance result from experimental artifacts.

Chapter 3

Conductance Switching in Single-Molecule Transistors Incorporating Bipiridyl Dinitro Oligo(phenylene ethynylene)

One area of strong interest within molecular electronics has been molecular switching, the experimental observation that conduction through some molecular systems has been observed to switch discretely between states of comparatively high and low conductance. Discrete switching has been observed in a number of measurement configurations and molecules [29]. Scanning tunneling microscopy (STM) has been particularly useful in studying this phenomenon by observing molecules of interest assembled at grain boundaries and defects in alkane self-assembled monolayers (SAMs). Of particular interest is voltage-driven switching, when sweeping a dc bias voltage beyond a threshold V_{on} triggers the transition to the higher conducting state. In some experiments, this enhanced conduction persists until the bias is reduced to $V_{\mathrm{off}} < V_{\mathrm{on}}$ leading to hysteretic current-voltage characteristics. Blum *et al.* examined this phenomenon in bipyridyl-dinitro oligophenylene-ethynylene dithiol (BPDN-DT) in 2005 [30] using STM, a crossed wire method [31], and a nanoparticle-based technique [32], finding similar switching characteristics in all three measurement approaches (see Fig. 3.1). This consistency suggests that the switching in this case is

intrinsic to the molecule/metal system, rather than an artifact of a particular measurement technique.

One suggested switching mechanism that has both motivated molecular design and been the focus of intense theoretical analysis is reduction of functional groups on the molecule [33]. Polaron formation is one way of potentially stabilizing this reduction. One model [34] suggests that strong coupling between an electronic level and a vibrational mode localized to the molecule can lead to a renormalization of that level to a lower energy when occupied. In this drastically simplified model, the molecule is treated as a quantum dot with one electronic level ε_0 coupled to a vibrational mode ω_0 and leads L and R. Representing the annihilation and creation operators for electrons on the molecule and in the contacts as $\hat{d}$ ($\hat{d}^\dagger$) and $\hat{c}_k$ ($\hat{c}_k^\dagger$), respectively, and using $\hat{a}$ ($\hat{a}^\dagger$) as the annihilation and creation operators of a vibrational quantum, the Hamiltonian in this model becomes:

$$\hat{H} = \varepsilon_0 \hat{d}^\dagger \hat{d} + \sum_{k \in \{L,R\}} \left(\varepsilon_k \hat{c}_k^\dagger \hat{c}_k + V_k \hat{d}^\dagger \hat{c}_k + V_k^* \hat{c}_k^\dagger \hat{d} \right) + \omega_0 \hat{a}^\dagger \hat{a} + M(\hat{a} + \hat{a}^\dagger)\hat{d}^\dagger \hat{d}$$

Here, $\varepsilon_0 \hat{d}^\dagger \hat{d}$ gives the energy due to the occupation of the molecular level, and $\varepsilon_k \hat{c}_k^\dagger \hat{c}_k$ is the energy due to the occupations of the leads. The terms $V_k \hat{d}^\dagger \hat{c}_k$ and $V_k^* \hat{c}_k^\dagger \hat{d}$ give the energy for an electron to tunnel onto and off of the molecule, respectively; $\omega_0 \hat{a}^\dagger \hat{a}$ is the total vibrational energy, and $M(\hat{a} + \hat{a}^\dagger)\hat{d}^\dagger \hat{d}$ describes the electron-vibrational coupling. The detailed evaluation of this Hamiltonian [35] is beyond the scope of this document, but in the limit of strong coupling between the molecule and leads, multiple local minima can appear in the total energy of the system as a function of the

25
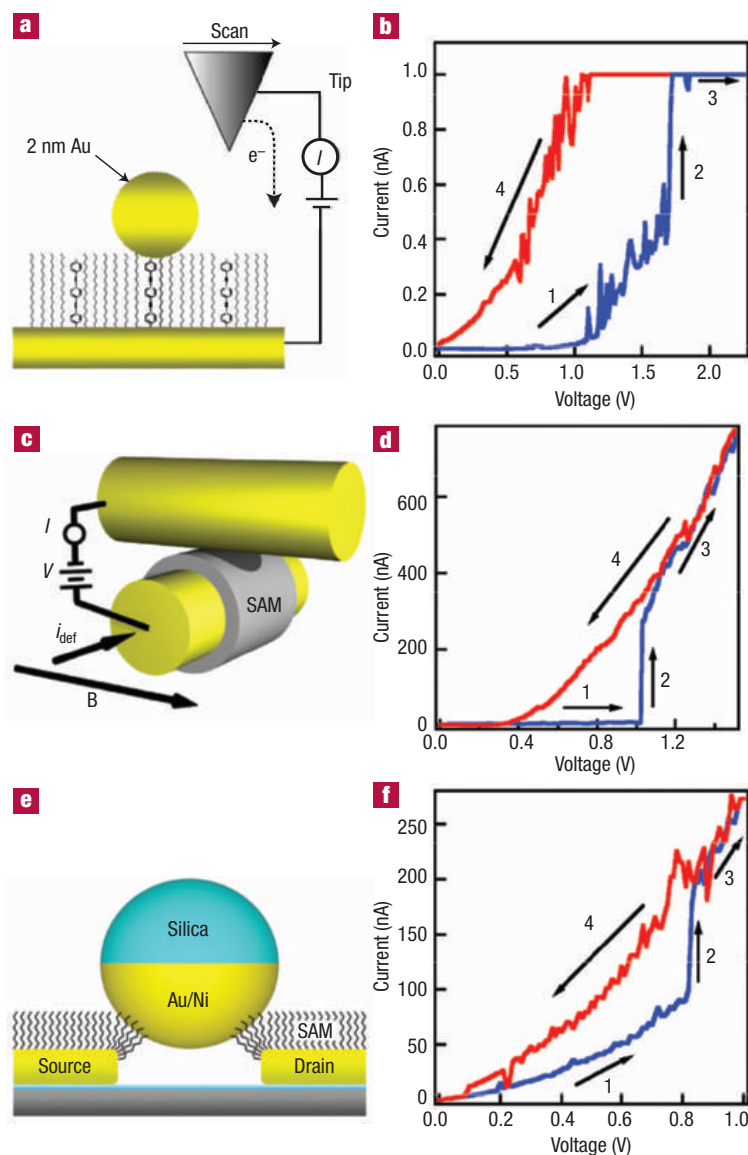
Figure 3.1 : Several measurement modalities for hysteretic conductance switching in BPDN (Adapted from [30]) (a) Diagram of STM-based I-V measurement. The tip is positioned over a single BPDN molecule in an alkanethiol matrix. (b) I-V curve of a single BPDN molecule measured in the geometry of (a). (c) Diagram of crossed-wire geometry for BPDN measurements. (d) I-V curve of a BPDN SAM measured in the geometry of (c). (e) Diagram of a magnetic bead junction. (f) I-V curve of a single BPDN molecule measured in the geometry of (e).

occupation of the molecular state [34]. In the context of switching, the physical idea is that large source-drain bias voltages can alter the average electronic population of the molecule from its zero bias value, and that excess charge can then be stabilized via this polaronic process, remaining on the molecule as bias is then reduced (see Fig. 3.2). There have been numerous theoretical examinations of such a model [34–39], with several reporting that bistable and hysteretic conduction can arise with certain ranges of parameters.

Other proposed switching mechanisms include macroscopic changes in molecular conformation [40], rotation of functional groups [41] or conjugated rings [42], bond fluctuation at the attachment point between the molecule and the electrode [43], and changes in hybridization between the molecule and the electrode [29, 44–46]. Since BPDN is a relatively short, highly conjugated molecule, however, changes in molecular conformation are unlikely, and there are no functional groups free to reorient themselves.

Single-molecule transistors (SMTs) can be used to examine candidate switching mechanisms. SMTs are three-terminal devices with conduction occuring between source and drain via a single small molecule, modulated by capacitive coupling to a proximal gate electrode. SMTs have been used to study other vibrational phenomena [47–52], and capacitive coupling to the gate has been used to manipulate the average electronic occupation of the molecules. As the gate voltage, V_{G}, is increased, the electrostatic interaction with the gate tends to favor an increased electronic pop-
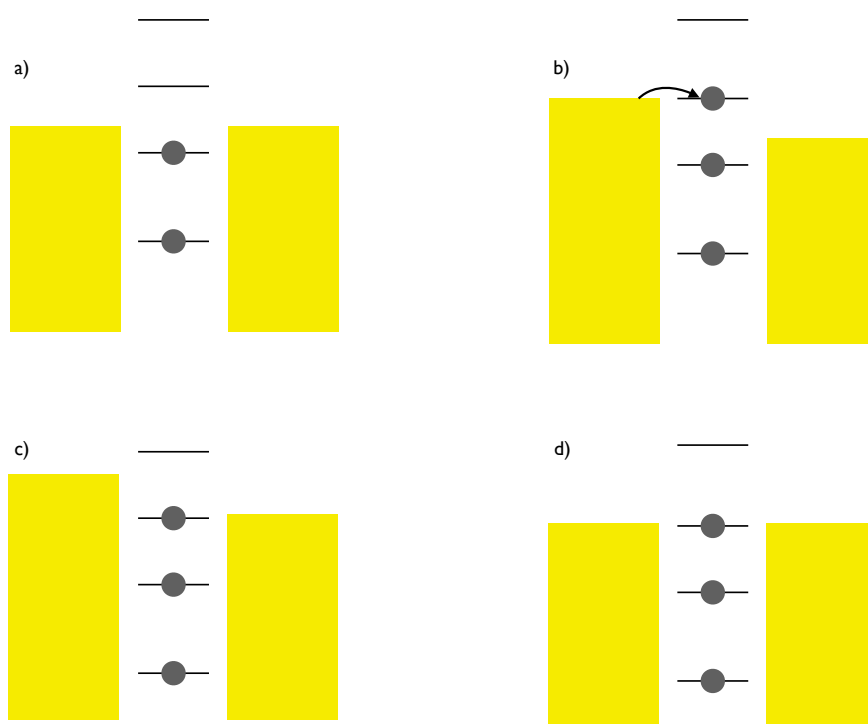
Figure 3.2 : Graphical representation of the hypothesized mechanism for polaron-mediated hysteresis. a) Ground state, $V_{SD} = 0$ b) As V_{SD} approaches V_{ON}, a molecular orbital is brought into resonance, and charge transfer occurs. c) Electron-phonon coupling shifts the manifold of molecular energy states, stabilizing the charge on the molecule. d) The charge, and the increased conductance, persist even with $V_{SD} < V_{ON}$.

ulation of the molecule. Therefore, in the polaronic picture, we would expect to see a tendency towards lower switching voltages as the gate potential is increased. By contrast, we would expect little to no effect from a gate if the switching mechanism involves changes in the molecule-electrode interaction. With this in mind, we fabricated and measured a large number of three-terminal devices to probe the origin of conductance switching in BPDN.

The fabrication of SMTs has been discussed extensively elsewhere [50, 53]. Using e-beam lithography, we define constricted wires on [100] $p+$ Si wafers coated with 200 nm of thermally grown SiO_2. Each wafer is patterned with at least 45 devices. Source and drain electrodes are 1 nm Ti/20 nm Au deposited by e-beam evaporation. After lift-off and O_2 plasma cleaning, devices are immersed in a 0.2 mM solution of acetate protected BPDN-DT [54] in a nitrogen-purged 1:1 mixture of THF and ethanol. Thiol-based self-assembly is carried out in the standard alkaline deprotection chemistry [55] for 48 h. Finally, the gold wires are electromigrated [21] to failure at 4.2 K, and electrical transport measurements are made as a function of source-drain bias, V_{SD}, and gate voltage, V_G at 10 K in a variable temperature vacuum probe station. The cryogenic environment minimizes the risk of adsorbed contaminants, and increases device geometric stability by inhibiting diffusion of metal atoms and molecules. DC measurements of device current-voltage characteristics $(I_D - V_{SD})$ are performed with the source electrode grounded, at various V_G. Initial post-electromigration characterization is via a source-drain bias sweep up to 100 mV.

The nanoscale variation between devices produced by the electromigration method necessitates a statistical approach to device characterization. Of 464 devices fabricated in this manner incorporating BPDN-DT, 169 exhibited no measurable tunneling current after electromigration. Previous experience and SEM imagery suggest that the most likely explanation is a resulting source-drain gap several nm or larger. All remaining devices found to have detectable conduction were measured at source-drain biases as high as 2 V.

These voltages are significantly higher than those used in previous experiments [50, 52, 56], and are necessary to search for switching phenomena like those reported for this molecule in other geometries [30]. For gaps in the range of 2 nm, the resulting source-drain electric fields at high bias can readily exceed the breakdown threshold of many materials. No sign of arcing or destructive irreversibility is observed in these devices after voltage application. However, a common failure mode of SMTs produced by electromigration is device instability: conductance characteristics that change irreversibly in the course of systematic measurements, presumably due to alteration of the device geometry (specifically the rearrangement of electrode atoms, or the breaking of the molecule/electrode bond). This instability is likely to be driven by both the electric field and the current density at the gap. These irreversible changes, which almost always result in lower overall conductance, make long studies at high biases very difficult.

Out of the devices with measurable conduction, 24 exhibited hysteretic behavior
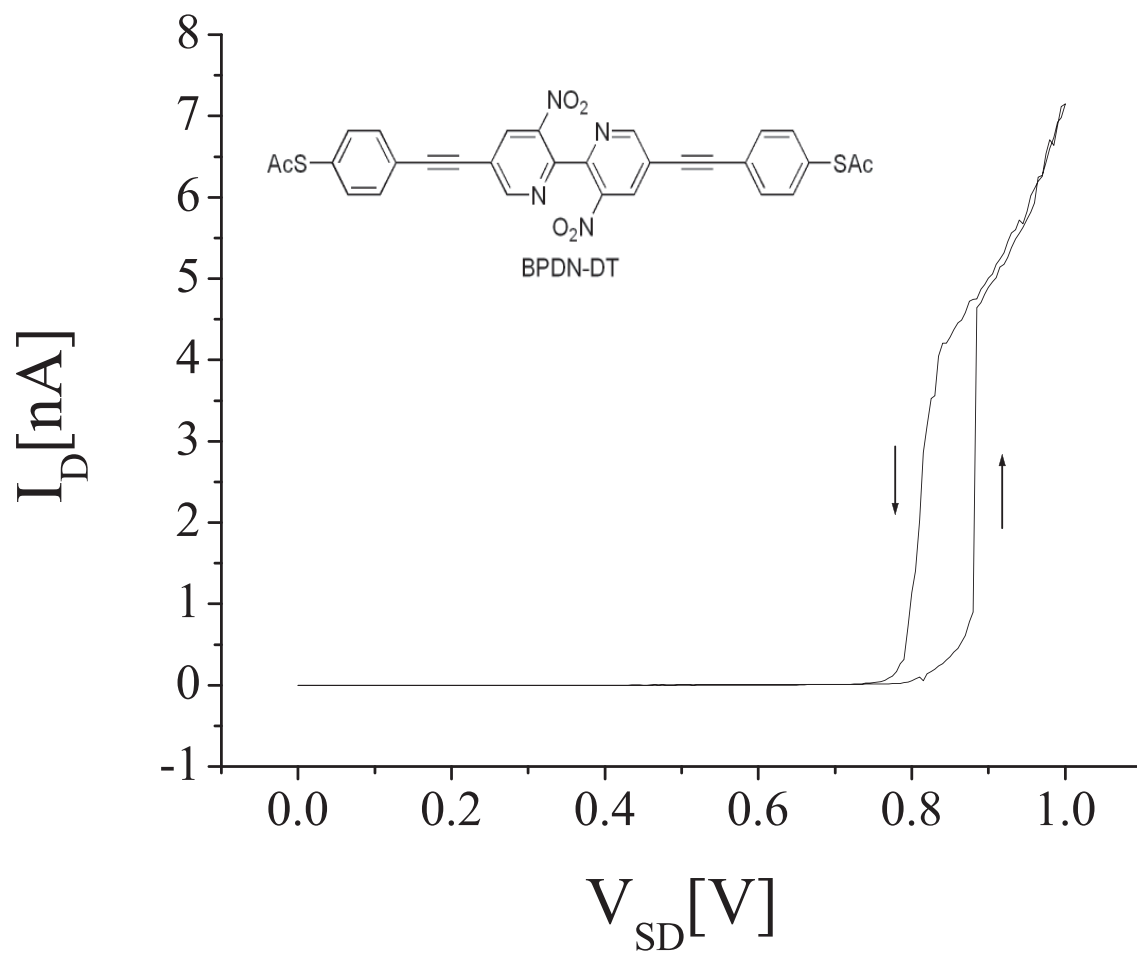
Figure 3.3 : I-V curve of a typical BPDN-DT device exhibiting conductance switching and hysteresis. Here, $V_{on} = 810\ mV$ and $V_{off} = 885\ mV$. Inset: Structure of the BPDN-DT molecule.

qualitatively like that shown in Fig. 3.3. The source-drain bias is swept from zero to a pre-defined endpoint (typically 1 V) in 40 s, then back to zero. Conductance is low ($< 10^{-8}$ S) until a characteristic threshold $V_{SD} \equiv V_{on}$ is reached. A discontinuous transition to a higher conductance state occurs; some devices exhibit regions of astability, in which several rapid transitions between the high and low conductance states occur, for V_{SD} just exceeding V_{on}. At higher biases, the device remains in the high-conductance state. As the bias is swept back down, the device remains in the high-conductance state until a second characteristic bias, $V_{off} < V_{on}$ is reached, at which point there is a transition back to the low-conductance state. In two additional devices, hysteresis was also observed, but with the opposite sense; that is, initial sweeps began in a more conducting state and at high biases a transition was observed to a less conducting state.

Control experiments were performed using both bare junctions and electromigrated junctions incorporating dodecanethiol ($C_{12}H_{25}SH$). Out of a total of 145 control device subjected to the same biasing scheme, no devices exhibited this hysteretic conduction. This is consistent with the BPDN-DT molecules being responsible for the hysteresis.

Both the switching voltages and the width (in V_{SD}) of the hysteretic region vary considerably from device to device. As shown in Fig. 3.4, V_{on} ranges from 390 mV to as high as 1.7 V, but in most of these devices is around 700 mV. This correlates well with previously reported results on voltage-controlled conductance switching in
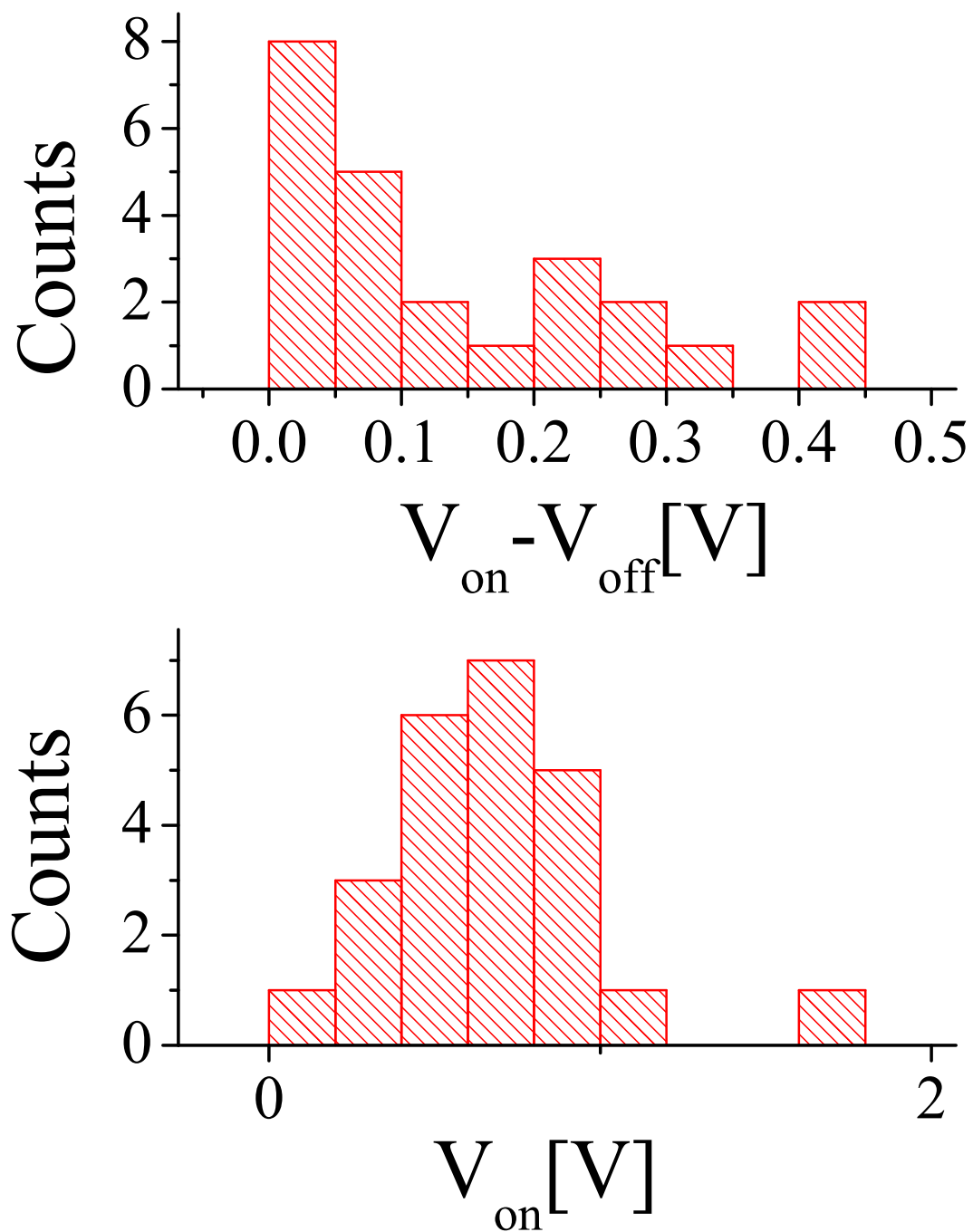
Figure 3.4 : Lower: Histogram showing the wide variability in V_{ON}. Upper: Histogram showing the variability in $V_{ON} - V_{OFF}$.

BPDN-DT [30]. The astability near the transition points between the two conductance branches further complicates attempts to quantify the width of the hysteresis. A hysteretic device under typical bias sweep conditions survives on the order of 10 bias sweeps (all showing hysteresis) before irreversibly changing to a lower conductance, non-hysteretic configuration, though occasional devices exhibited much better stability, surviving hundreds of cycles.

In addition to the source and drain, the BPDN-DT molecules in our devices are capacitively coupled to a gate electrode. The effective strength of this coupling depends strongly on the geometry of the junction, and the strength of the coupling between the molecule and the electrodes. In previous SMT experiments we have examined thousands of devices, and found that approximately 10-15% of the initially patterned electrodes show significant gate dependence. This is true both for physisorbed molecules (C_{60}) [50,53] and transition metal complexes attached via gold-thiol bonds [52,56]. In the BPDN-DT devices examined, only two out of the original 464 devices show any systematic gate dependence; Fig. 3.5 shows a set of $I_D - V_{SD}$ curves from one of these devices.

Detailed studies of the gate dependence (*e.g.* the conductance maps as a function of V_{SD} and V_G familiar from Coulomb blockade devices) were impeded by the short device lifetime described above. However, it was possible on the other gate-dependent device to sit at a bias near V_{ON} and sweep V_G, to search for any systematic variation of V_{ON} with gate potential. The data are shown in Fig. 3.6. The device shows
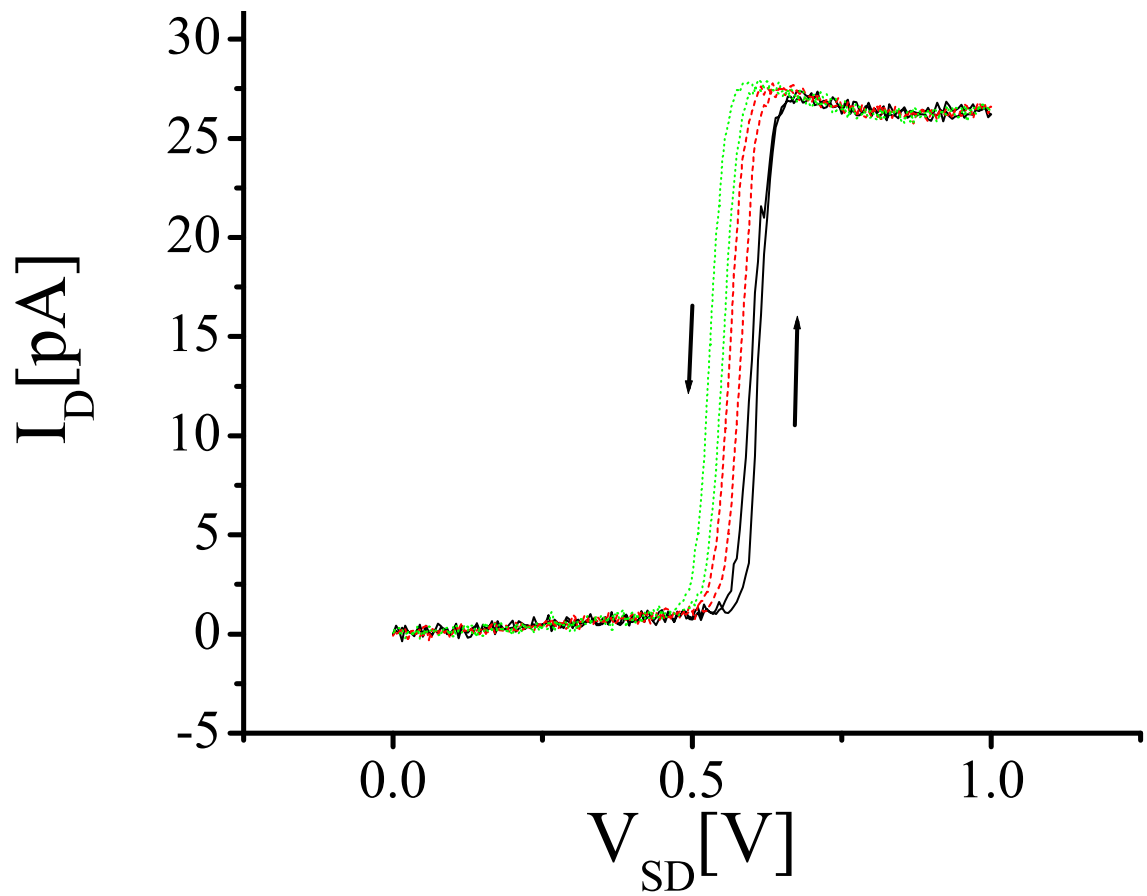
Figure 3.5 : Gate dependence of one BPDN device. Moving from left to right, the curves represent $V_G = +40$ V (green, dashed), 0 (red, dotted), and -40 V (black, solid), respectively. Arrows indicate the sense of the hysteresis for each curve.

sporadic, hysteretic switching between conductance states as V_{G} is varied, with a weak, nonmonotonic trend toward lower conduction at more positive V_{G}. Note that this is the *opposite* trend as that seen in the device of Fig. 3.5.
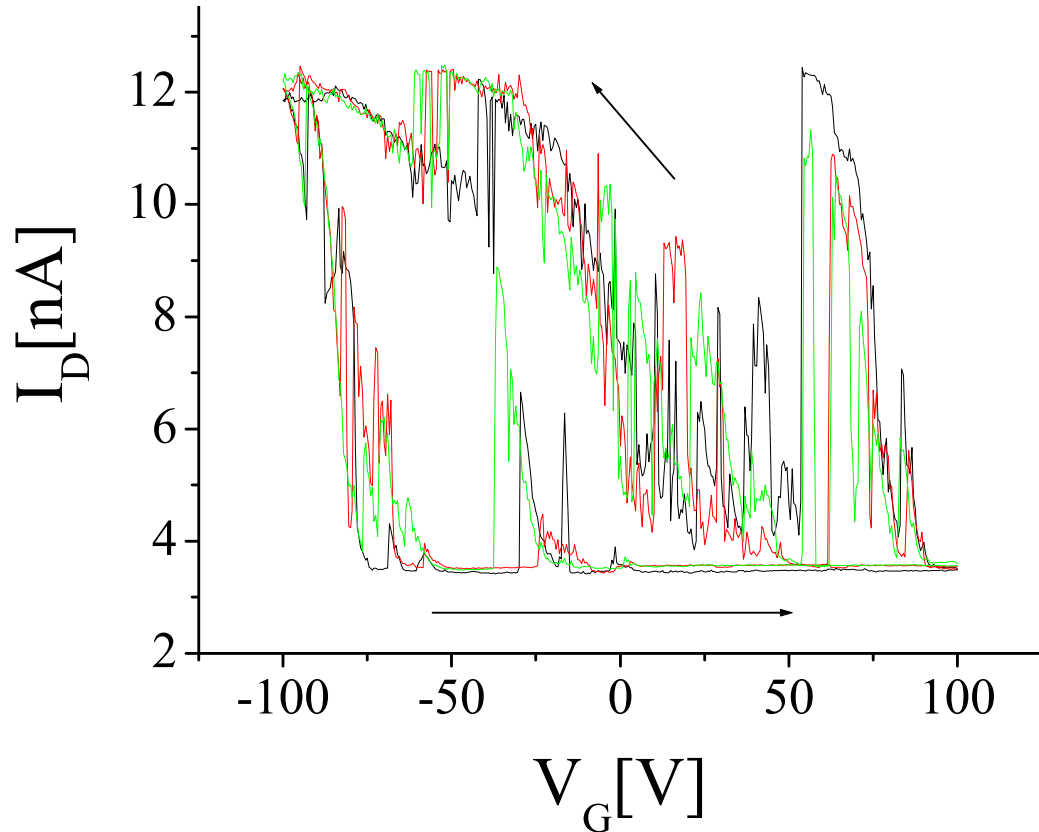
Figure 3.6 : Current through a BPDN device as a function of V_{G} with $V_{\mathrm{SD}} = 600\,\mathrm{mV} \simeq V_{\mathrm{ON}}$. This device was measured starting at $V_{\mathrm{G}} = +100$ V, sweeping down to -100 V and back several times.

These data constrain the switching mechanism discussion significantly. If the source of the hysteresis is an electronic effect such as polaron formation, one would expect a reproducible, systematic trend of V_{on} with V_{G}. An increasingly positive V_{G} acts to stabilize additional electronic population on the molecule, presumably lower-

ing the source-drain bias required to populate the next electronic level. The efficiency of gate coupling in previous SMT devices with this oxide thickness [50,52,56] has generally been on the order of a few percent, implying that a 100 V swing of V_{G} should systematically shift molecular levels (and correspondingly V_{on} and V_{off}) by a few hundred meV. Whether this is sufficient to bring a molecular level into alignment with the source/drain chemical potential depends on the details of the molecule's electronic structure (gap between highest occupied and lowest unoccupied molecular orbitals) and the molecule-metal bonding. Further, while transport via highest occupied *vs.* lowest unoccupied orbitals could affect the sign of the gate trend, the differences between Figs. 3.5 and 3.6 would imply that qualitatively identical transport in different devices takes place through different orbitals, which seems unlikely.

Within the polaronic picture of hysteresis, which implies that the energetic difference between the source/drain chemical potential and a molecular orbital is $\sim eV_{\mathrm{on}}$, there are limited possible explanations for the observed weak gate coupling. If this particular molecule self-assembles or moves during electromigration in a manner very different than in other experiments, it is conceivable that there could be a systematic trend toward device geometries with weak gate couplings. This seems unlikely, given the relatively ordinary self-assembly properties of BPDN-DT reported by Blum *et al.* [30]. Very strong electronic coupling of the BPDN-DT molecules to at least one of the electrodes could also explain a relatively weak effect of the gate. If the molecular levels are strongly pinned relative to the Fermi level of a lead, then effectively the

molecule will be screened well from the gate potential. Such a strong lead coupling would strongly constrain dynamic polaron formation, requiring weak gate coupling, yet a large enough reorganization energy that small bias-driven charge transfer could shift the level into or out of resonance, all relatively independent of the details of the Au site to which the molecule is bound. Detailed quantum chemistry calculations should at least be able to assess the likelihood of such strong coupling between the molecule and the metal, as well as the level alignments mentioned above.

A more plausible explanation, in our view, is that the switching mechanism in these devices is based on bias-driven changes in the molecule/electrode hybridization or bond angle, rather than a direct electronic process like polaron formation. The lack of gate dependence would then naturally follow from a large energetic difference between molecular levels and the source/drain chemical potential. Given the heterogeneous environment of the electromigrated junctions, it would not be surprising for the molecule to bind asymmetrically to the electrodes. Indeed, during initial SAM formation, only one end of the molecule is expected to be bound to the Au surface. Under this circumstance, the bound molecule can acquire a net electric dipole moment, which may be enhanced by the strong electron-withdrawing character of the nitro groups in BPDN-DT. STM experiments have already demonstrated [44] that electric dipoles can lead to a bias influence on conductance switching in other molecules, which has been interpreted as due to changes in molecule/electrode hybridization [29, 44]. Interestingly, switching behavior has been studied in some detail

in oligo(phenylene vinylene) molecules, where lower voltage thresholds for switching enable significantly easier data acquisition [57]. The suggested mechanism in this case involves breaking and reformation of a S-H bond near the contact. While it is not clear to what extent the feasibility of this mechanism depends on the details of the nearby dielectric, it is certainly likely that the details of the contacts play a role in the electronic behavior.

We have performed measurements of electromigrated junctions in a SMT configuration incorporating BPDN-DT, a molecule known from other experiments to exhibit hysteretic conductance switching as a function of V_{SD}. We observe similar hysteretic characteristics that are absent in control devices not incorporating the molecule of interest. The dependence of the conductance on V_{G} is much weaker than observed with other molecules in SMT experiments. We find that there is no evidence for the polaron-mediated hysteresis hypothesis; indeed, a much more likely explanation, in our view, is that the hysteresis depends on the geometry of the molecule/metal interface. In effect, the molecule may physically behave like a mechanical switch.

It may be of some minor interest to note that an experiment carried out using an STM tip to contact BPDN molecules in an electrochemically active liquid environment has given an indication that charge transfer onto the molecule could play a role in the conductance switching [58]. It is clear that, in this case, a change in the potential of the electrolyte led to reversible, hysteretic conductance changes in the neighborhood of the molecule; however, due to the possible presence of counter ions,

relatively poor signal to noise, and signs of irreversibility in that system, this analysis may be regarded as less than definitive. Quantum chemistry calculations in highly simplified models have also yielded a diversity of predictions regarding the origin of these switching behaviors [35,59,60]; it may be of interest to perform more detailed *ab initio* calculations to further elucidate the possible mechanisms for this effect. While we find no support for the polaron hypothesis in this system, there are many other molecules known to have strong electron-phonon coupling [61], and it is certainly possible that polaron-mediated hysteresis may appear in these other systems. Given the relative uncertainty that continues to surround this area of inquiry, performing SMT experiments using molecules known to have strong polaron formation tendencies remains an interesting direction to pursue.

Chapter 4

Electronic Noise in Atomic-Scale Structures

4.1 Overview of noise processes

Noise is most often viewed as an impediment to effective measurements. Techniques such as lock-in measurements have been devised to eliminate noise from periodic signals, and there are entire volumes published on other active and passive noise reduction methods. However, the specific character of electronic noise, and the conditions under which it appears, can also yield useful information about the details of electron transport in nanoscale systems. This chapter explores some of the ways that noise can reveal details not evident in other measurement modalities, presents a highly-sensitive system for measuring electronic noise in single-molecule transistors, and discusses some early data from such a system.

There are three categories of noise directly relevant to this investigation: Johnson noise, 1/f noise, and shot noise. Johnson noise, discovered in 1928 [62], arises from the thermal motion of charge carriers in a resistive element [63]. It is characterized by a flat power spectral density, and appears in any resistive system at finite temperature. 1/f noise is characteristic of semiconductors and disordered metals, and can arise from generation-recombination noise, universal conductance fluctuations, or any of

several other processes. Generally, it does not appear in the absence of a dc current.

Shot noise arises from the discrete nature of the charge carriers in material systems.

Because charge is quantized (generally in units of e), and because the arrival times of

carriers follows a Poissonian distribution in the absence of intertemporal correlations

between the carriers, there are fluctuations in the measured current in, e.g., tunnel

junctions. These fluctuations depend only on the unit of charge and the average

current through the device, and they produce a current noise with a flat power spectral

density.

4.1.1 Johnson-Nyquist noise

J. B. Johnson first described the thermal fluctuations of electric charge in conductors

in 1928, using a vacuum-tube amplifier, a variable tank circuit, and a thermocouple to

measure the noise power [62]. He found that, in a wide variety of resistive materials,

and over the temperature range from liquid nitrogen to boiling water, a noise power

was generated proportional to the temperature and the resistance:

$$(S_V)^2 = 4k_B T R \tag{4.1}$$

Here, S_V is the noise voltage spectral density, $k_B = 1.38 \times 10^{-23} \frac{J}{K}$ is the Boltzmann

constant, T is the absolute temperature, and R is the resistance. Later that year,

Nyquist presented a theory of thermal noise based on thermodynamics and statistical

mechanics [63].

Nyquist's explanation of thermal noise is strking in its simplicity and elegance.
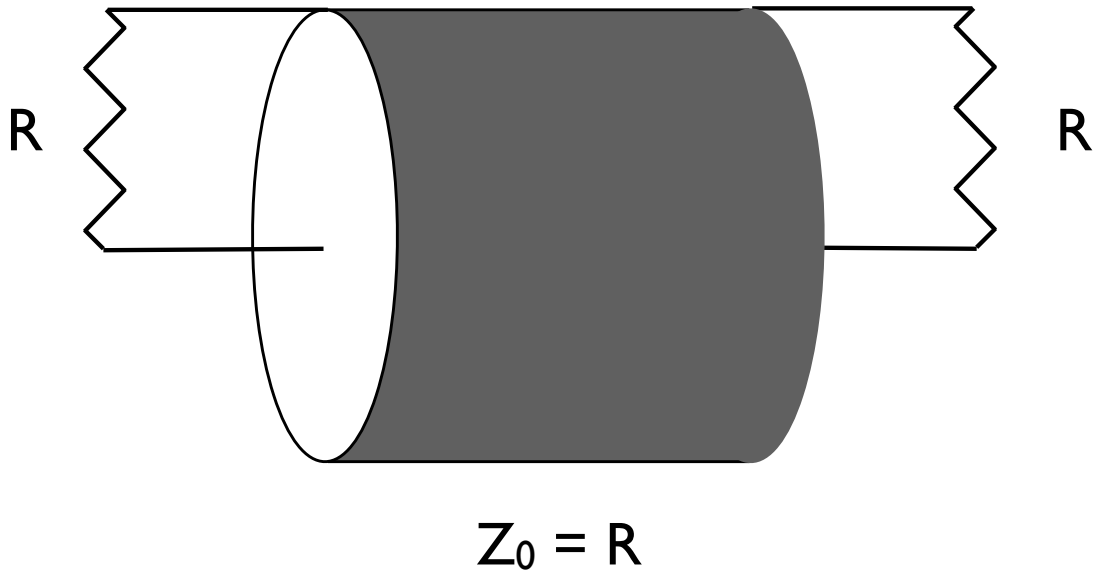
Figure 4.1 : Illustration of a thought experiment for Johnson noise

Consider the circuit of Fig. 4.1: a pair of matched resistors R_L and R_R, each with re-sistance R, are connected by a lossless transmission line with characteristic impedance $Z = R$. Since the loads at either end are matched to the line, an electrical signal propagating in either direction will be completely absorbed in the load resistance — there will be no reflection. If the system is in thermal equilibrium, the temperatures of the two resistances will be equal:

$$T_L = T_R = T. \tag{4.2}$$

The thermal fluctuations of charge in R_L will then produce a rightward-moving signal on the line, which is absorbed in R_R, and vice versa.

Imagine replacing the resistances R_L and R_R with short circuits at either end of

the line. We now have a one-dimensional electromagnetic cavity, perfectly reflecting at both ends, with length L and propagation velocity v. Since the transmission line has a finite velocity of propagation, some energy will have been trapped in the cavity. This cavity will have a discrete spectrum of electromagnetic modes, each with frequency $f_n = \frac{nv}{2L}$. In the low-frequency limit $hf \ll k_B T$, the equipartition law gives the energy in each mode as $k_B T$. The energy trapped in the cavity within a frequency range ΔF is then proportional to the number of modes within that frequency range:

$$E = k_B T \frac{\Delta F L}{v}. \tag{4.3}$$

Equation 4.3 represents the total energy in the cavity; we want to find the average power generated by the thermal noise of the resistances. Recall that our initial scenario involved resistances matched to the transmission line, so that there would be no reflection at either end. The energy trapped in the cavity must then only be that which was generated by the resistances in the time interval $\Delta t = \frac{v}{L}$. We can divide the energy in the cavity by this time interval to obtain the average power:

$$P = k_B T \delta F. \tag{4.4}$$

One of Ohm's three laws gives the relationship between the current in the transmission line and the voltage across the resistors:

$$I = \frac{V}{2R}. \tag{4.5}$$

Using the relationship $P = I^2 R$ and some simple arithmetic, we then obtain Johnson's

experimental result for the noise voltage in a frequency interval Δf:

$$V^2 = 4k_B T R \Delta f. \tag{4.6}$$

As a final note, most interesting single-molecule systems have nonlinear conduction as a function of bias voltage. In these cases, the relevant "resistance" for the purposes of Johnson noise is not $\frac{V}{I}$, but rather the differential resistance $\frac{dV}{dI}$.

4.1.2 Shot noise

As stated above, shot noise is a result of the discrete nature of charge carriers. One way to describe the electronic transport through a tunnel barrier is by the average current $<I>$. This doesn't fully capture the character of the current, however, because the arrival times of the individual carriers cannot be determined from the average current. Instead, different numbers of carriers arrive and cross the barrier in different time intervals. Assuming that the arrival times of the electrons are random (i.e. governed by a Poisson distribution), this leads to a fluctuation proportional to the amplitude of the current:

$$S_I = 2eI \tag{4.7}$$

It should be noted that this expression is valid only in tunneling barriers with a low transmission probability. In the context of atomic-scale constrictions, the math gets more complicated. Consider the case of a single perfectly-conducting channel — for example, a single-atom constriction in a gold nanowire. The Pauli exclusion principle dictates that the arrival times of the electrons in such a system will be evenly spaced

in time, which minimizes the current fluctuations. Poissonian statistics no longer describe that system, and so the shot noise differs from the classical prediction. In the case of a mesoscopic system at zero temperature consisting of several channels, each with transmission coefficient T_n, the Landauer formalism gives the total conductance

$$G = \frac{2e^2}{h} \sum_n T_n \tag{4.8}$$

and the shot noise is given by the Büttiker formula

$$S_I = 2eV(\frac{2e^2}{h}) \sum_n T_n(1 - T_n). \tag{4.9}$$

At finite temperature, things get more complicated, in that the Johnson noise and shot noise interact [64]:

$$S_I = 4kT(2e^2/h) \sum_i T_i^2 + 2eV(2e^2/h)coth(eV/2kT) \sum_i T_i(1 - T_i). \tag{4.10}$$

Fortunately, at low temperatures and high bias, this reduces to the familiar Schottky result.

Another interesting case to consider is a situation in which the electrons are positively correlated with each other. For example, in the BCS theory of superconductivity, electrons form Cooper pairs, quasiparticles with a charge of $2e$. It is, then, perhaps unsurprising that the shot noise in a superconducting-normal tunnel junction is twice the Poissonian result [65]; we see that a primary determinant of the magnitude of shot noise is the effective charge of the carrier, rather than the fundamental electric charge e. It is convenient to define the Fano factor F as the ratio
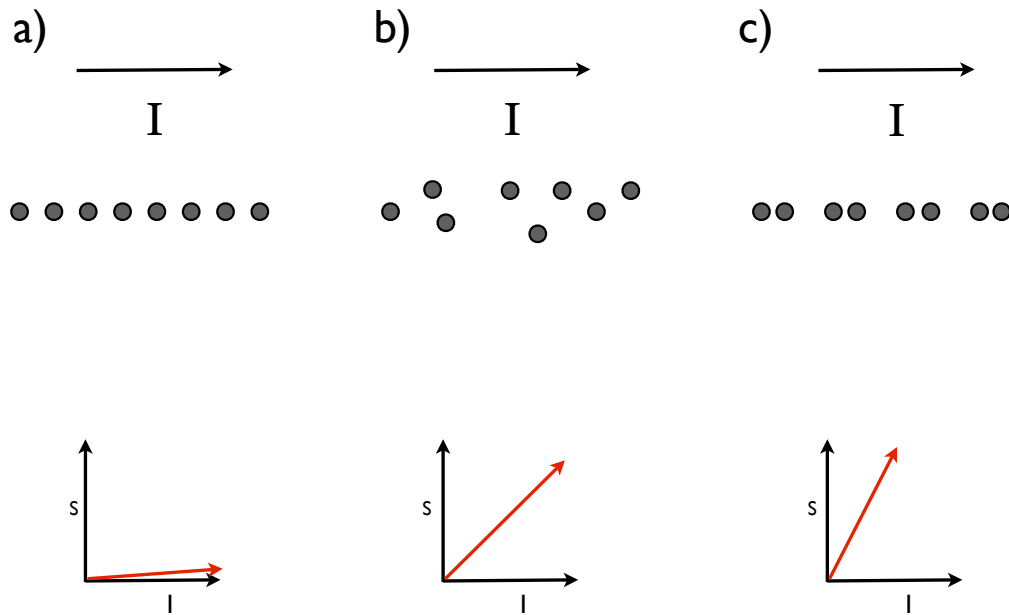
Figure 4.2 : Graphical representation of three cases for shot noise. (a) Carriers are anticorrelated in time; $F \ll 1$. (b) Carriers are uncorrelated in time; $F = 1$. (c). Carriers are positively correlated in time; $F = 2$

between the observed shot noise and the Poissonian figure. Figure 4.2 graphically represents the cases of suppressed, Poissonian, and enhanced shot noise.

In the case of a single-molecule transistor, it is of particular interest to study shot noise in the Kondo regime. The Kondo effect is a case of strongly correlated electron physics. It requires a quantum dot with an unpaired spin, coupled to source and drain electrodes with many free spins. In the single-molecule case, a singly occupied d orbital may lie below the Fermi level of the source and drain leads. While

the on-site repulsion may classically forbid double occupation of the atomic orbital, it is nevertheless possible to form a virtual state in which a second electron, with spin opposite the first, tunnels onto the dot from the source electrode. The first electron may then tunnel out onto the drain electrode, restoring the system to an energetically favorable state, but with the unpaired spin opposite that of the original state. Phenomenologically, this is manifested as a temperature-dependent enhanced molecular conductance at zero bias in dc measurements, but the required correlations between the electrons have also led to theoretical predictions of enhanced shot noise in these systems [66–68].

Another situation which may yield enhanced shot noise is Franck-Condon blockade, which occurs in molecules with strong electronic-vibrational coupling and long vibrational relaxation times. In the blockaded regime, electron transport is expected to be avalanchelike, with large bunches of electrons crossing the molecule only when a phonon is excited. Once the first electron crosses the molecule via vibration-assisted tunneling, the energetics are such that a transition to a higher vibrational energy state becomes increasingly likely; this repeats with each phonon excited on the molecule, leading to electrons transiting the molecule in large bunches. A Monte Carlo simulation with reasonable parameters can yield Fano factors of over 1000 in this case [69]. One goal of this experimental program is to test these predictions.

4.2 Experimental considerations for shot noise measurement

Shot noise can be a very difficult signal to measure effectively, as it is a small, frequency-independent signal. There have been several experimental efforts to measure shot noise in quantum dots, and they fall into three categories. In the first, the current through a quantum dot is modulated at audio frequency, the resulting radio-frequency noise is passed through a bandpass filter, to define a known noise bandwidth for a measurement, and then the total noise power over that band is detected via a lock-in technique(see Fig. 4.3). The total power can then be divided by the equivalent noise bandwidth to determine the power spectral density, and the Fano factor can be obtained from that figure. While this is probably the most straightforward possible measurement technique, and it has the advantage of rejecting any constant interfering signals, such as Johnson noise, it loses any information about the spectrum of the noise — one must assume that the input is frequency-independent. A second measurement technique involves a tank circuit adjacent to a quantum dot, feeding a transconductance amplifier at frequencies around 1-2 MHz [64, 70]. A pair of independent cryogenic amplifiers is then placed in close proximity to the tank, in order to minimize losses in the transmission line; a further amplification stage conditions the signal at room temperature; and the signal can be digitized and cross-correlated to suppress amplifier noise (see Fig. 4.4). Finally, the time series is Fourier transformed to extract a frequency spectrum. A model of the tank circuit is then used to calculate the equivalent white noise power spectral density. The primary advantage of this
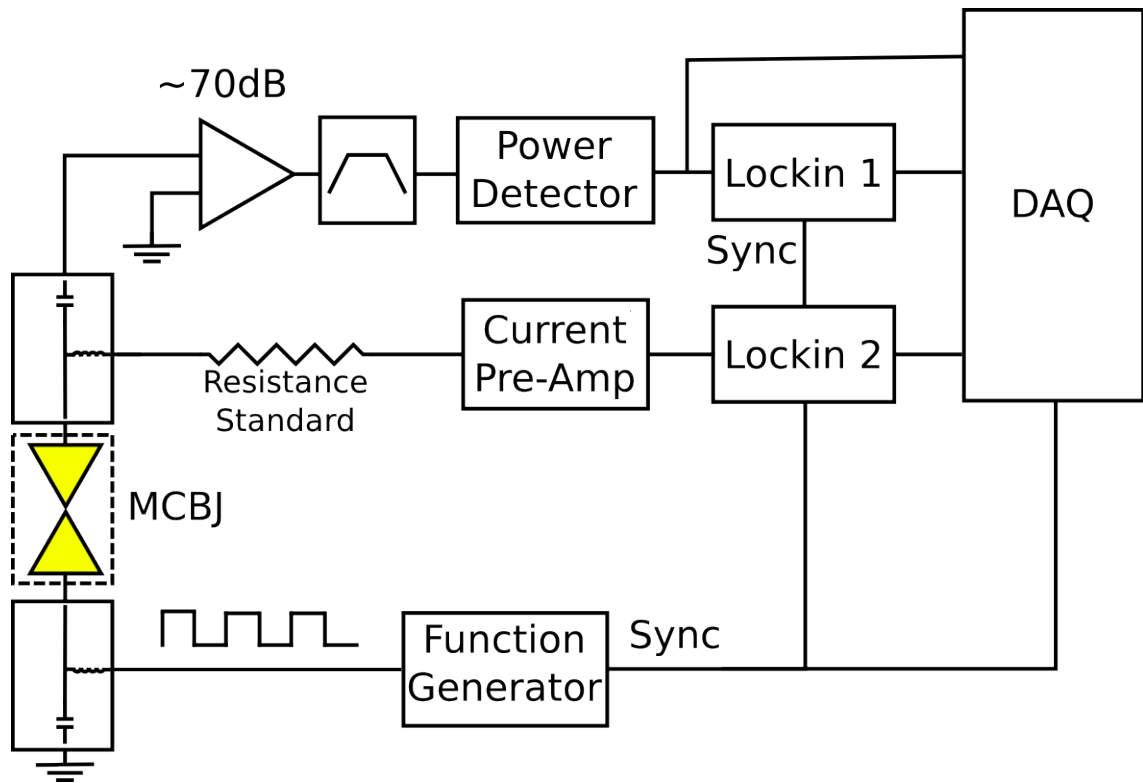
Figure 4.3 : Block diagram of a scheme for measuring shot noise at high frequencies via lock-in technique.
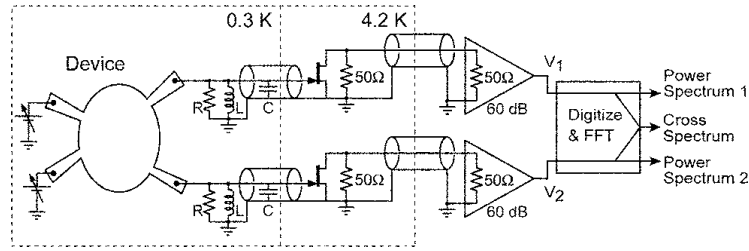
Figure 4.4 : An experimental setup for measuring cross-correlated current noise around 1 MHz (adapted from [70]).

technique is that low-noise amplifiers based on 2-d electron gases in gallium arsenide are commercially available and capable of operation at low temperatures. However, it is necessary to have a cryostat capable of accommodating a cryogenic amplifier, as well as high-speed digitizing hardware; these are not necessarily available in every lab.

The technique employed for this investigation is somewhat analogous to that of [70], but due to hardware constraints, we carry out the entire measurement in the DC-100 kHz band. A metallic constriction or single-molecule transistor is fabricated by electromigration, and the noise voltage across the device is measured by a set of independent, matched low-frequency amplifiers. The resulting amplified signals can then be cross-correlated to eliminate the amplifier noise, and Fourier transformed to extract a frequency spectrum. A bias current can be applied by way of a cold resistor (see Fig. 4.5). The advantage of this technique is that it leverages our hardware and experience with near-DC measurement techniques; additionally, at the relatively low frequencies used in this experiment, signal attenuation in the cabling is less of an
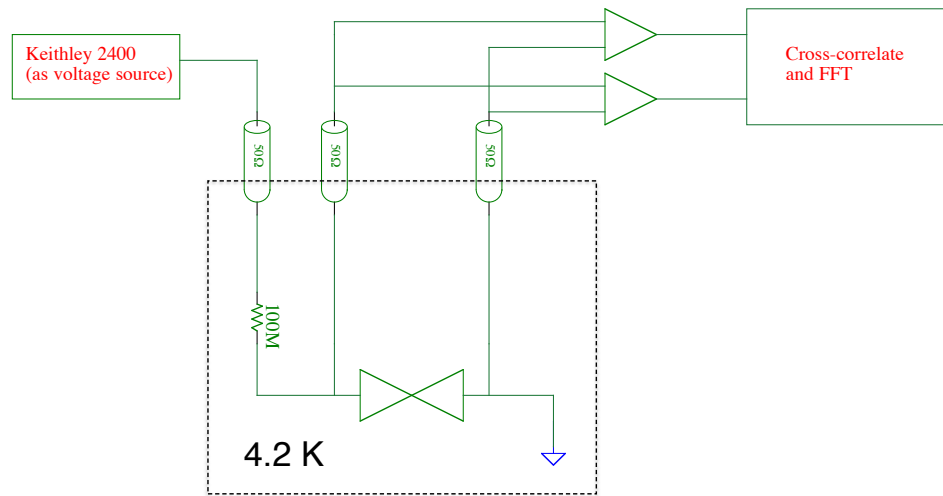
Figure 4.5 : Scheme for cross-correlated noise measurements at low frequency

issue than it would be at RF.

Our first measurements using this setup were carried out in a variable-temperature cryostat from Quantum Design. Unfortunately, this cryostat is poorly suited to the sort of high-throughput testing necessitated by our relatively low-yield fabrication techniques, and the electrical design is far from optimal for low-noise measurements. We have had better luck with a cryogenic four-probe station from attocube systems. The movable-probe design is ideal for contacting and measuring large numbers of
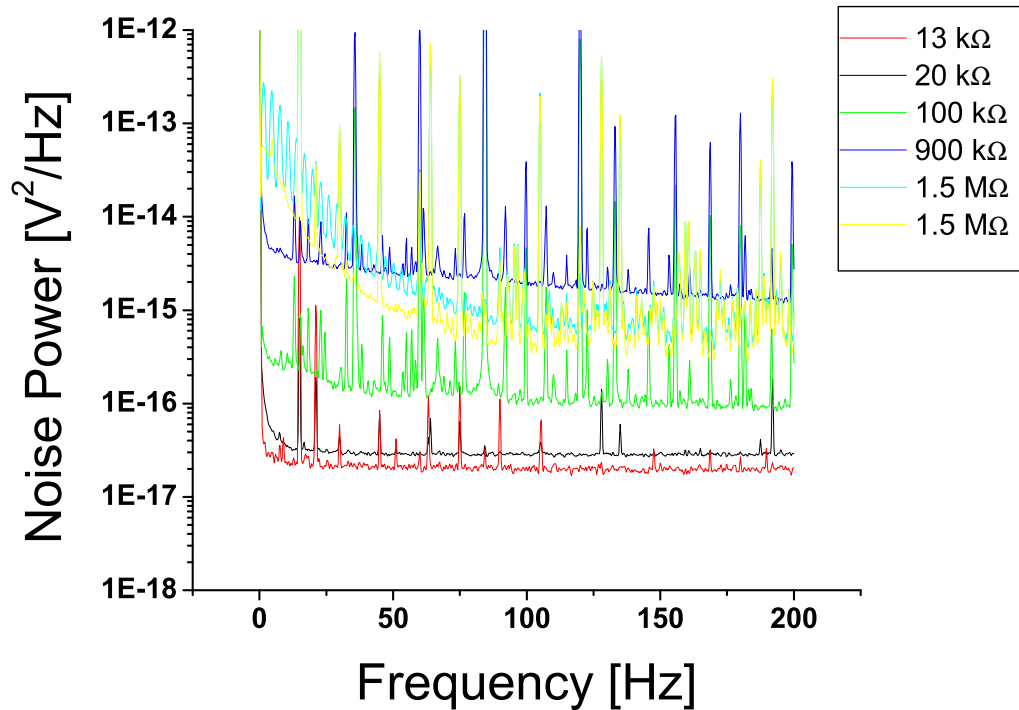
Figure 4.6 : Low-frequency noise spectra of an electromigrated device at 10 K and zero bias, at several different resistances. Note the large number of peaks extrinsic to the device, as well as the appearance of $1/f$-like noise at higher resistances.

devices, and the internal signal paths consist entirely of 50Ω coaxial cable, which is a great help for noise reduction. Still, there are considerable technical impediments to the collection of high-quality data in this system. Multiple harmonics of 60 Hz and, oddly, 48 Hz, are evident in the low-frequency data (see Fig. 4.6), while attenuation in the cabling inhibits high-frequency data collection from high-impedance devices. A further issue is the impedance and noise characteristics of the input stages of the amplifiers. Initially, we used amplifiers optimized for low voltage noise, with

correspondingly low input impedances and high current noise. As it turns out, these designs were optimized for devices with output impedances ~ 1 kΩ — far from even the most highly conducting single-molecule devices. Eventually, we determined that no commercial amplifier met our requirements of low current noise and high input impedance, and so it became necessary to build custom voltage amplifiers. These amplifiers are designed to have variable gain from 100 to 10^4, and details of their design, construction and characterization are in appendix C. Surprisingly, the transition to completely battery-powered amplifiers did not eliminate the harmonics of 60 Hz, but the high-impedance amplifiers did facilitate the acquisition of fairly clean noise data at higher frequencies. The initial test of the new amplifiers was the collection of Johnson noise. Fig. 4.7 shows noise spectra for a 13 kΩ device, as well as fits to a low-pass filter function characteristic of the cabling in our cryostat. Fig. 4.8 shows the temperature dependence of the fitted noise power, as well as the value for Boltzmann's constant ($= 1.34 \times 10^{-23} \frac{J}{K}$) extracted from these fits. These figures demonstrate that the noise floor of our entire system, with cross-correlation in place, is significantly lower than the $\sim 10 \frac{nV}{\sqrt{hZ}}$ voltage noise of our amplifiers. This in turn demonstrates that amplifier noise suppression via the cross-correlation technique is effective in our system, and that we can expect to see shot noise in appropriate devices.

The goal of this experimental program, of course, is to measure shot noise in single molecules, both in and out of the Kondo regime, and to thereby verify or falsify the theoretical predictions of an enhanced Fano factor for the Kondo conduction
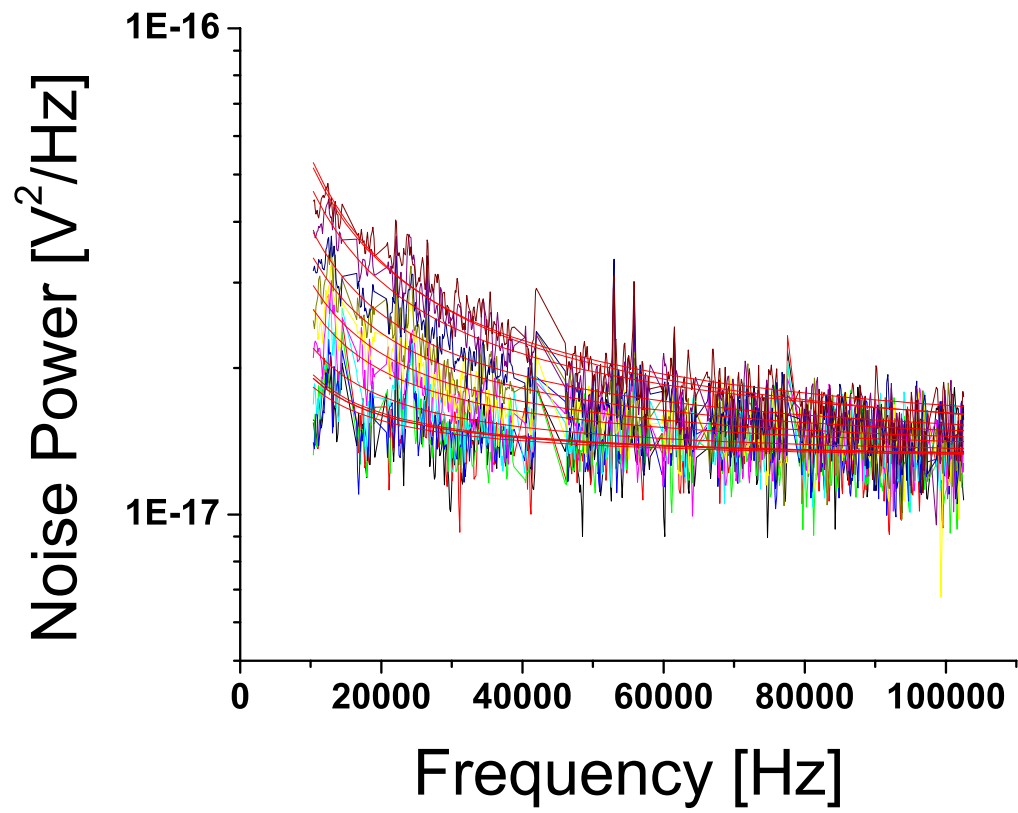
Figure 4.7 : Johnson noise of a 13 kΩ electromigrated device, and least-squares fits to the low-pass filter characteristic of our system
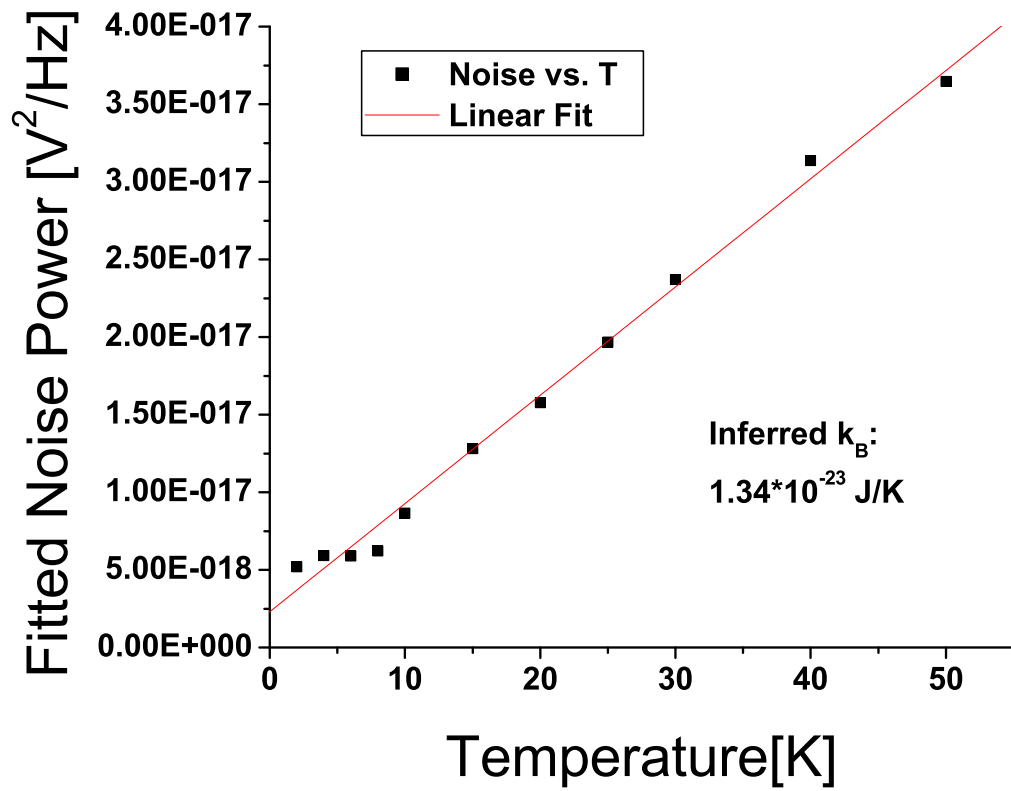
Figure 4.8 : Noise power spectral densities extracted from the fits to Fig. 4.7, as well as a fit of the temperature dependence. The implied value of k_B is $1.34 \times 10^{-23} \frac{\text{J}}{\text{K}}$.

process. To that end, we have measured data on the current dependence of one device incorporating a highly-conjugated tetragonal cobalt complex. This molecule has been shown to exhibit the Kondo effect in previous experiments. This device was broken to a zero-bias resistance of ~ 100 kΩ and biased with a room-temperature voltage source and a 100 MΩ cryogenic resistor. The raw data, some of which are shown in Fig. 4.9, show that, while Johnson noise is certainly present at zero bias, there is a strong bias-dependent component to the noise. While the functional forms of these noise spectra are complicated, and not amenable to fitting without an outlandish number of parameters, it is possible to look at the noise power averaged over a finite bandwidth (Figs. 4.10 and 4.11). This shows a clear trend towards greater noise at higher bias currents, and it is likely that, with higher-quality data and further testing, a Fano factor for this type of device could be determined.

4.3 Outlook and conclusions

In conclusion, this chapter seeks to elucidate some of the technical challenges inherent in single-molecule shot noise measurements, and to point out some possible pathways towards a solution to these challenges. It is clear that high-input-impedance voltage amplifiers will be critical to any successful effort to make further noise measurements on single-molecule devices. While signal attenuation in the cabling remains a significant issue, there are some ways to ameliorate this problem. The most obvious of these is to shorten the cabling, but that is not always possible, given the demands
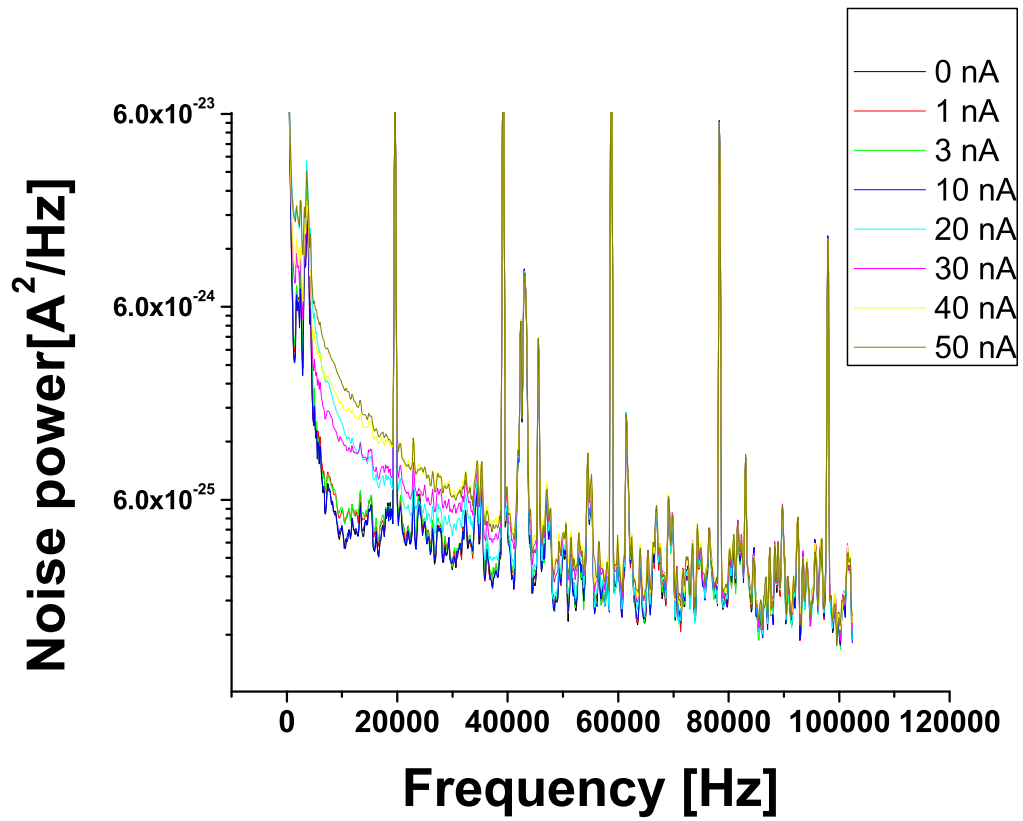
Figure 4.9 : Noise power spectra for a 100 KΩ device at several values of bias current. Note the strong current dependence, as well as the unusual functional form of the spectra.
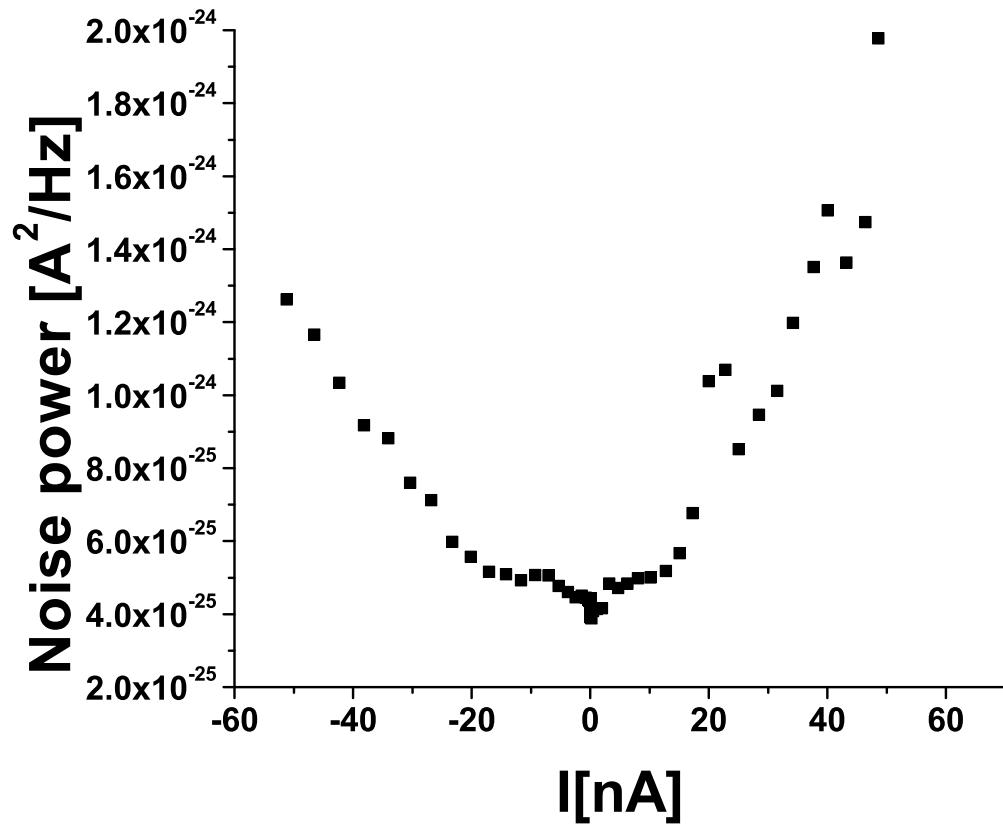
Figure 4.10 : Average noise power vs. bias in the band from 10 to 18 kHz.
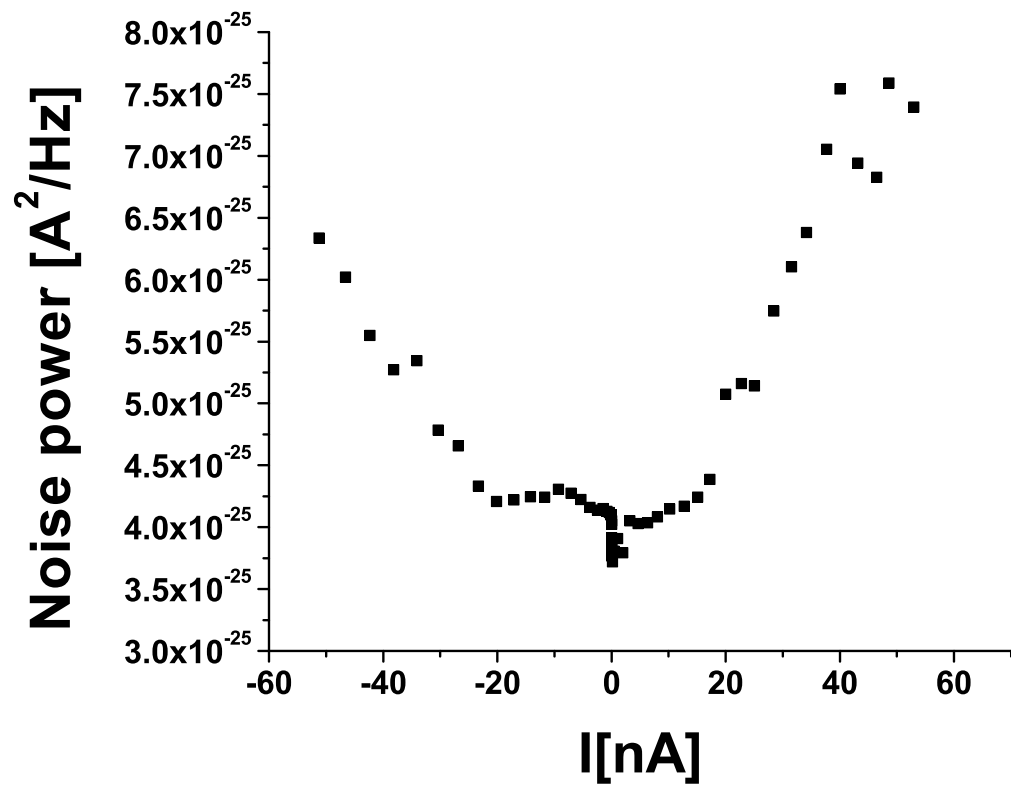
Figure 4.11 : Average noise power vs. bias in the band from 22 to 35 kHz.

of cryogenic operation. Another possibility is to employ cryogenic amplifiers, which can easily be placed in close proximity to the signal source. Unfortunately, silicon, which is the basis for all current low-frequency amplifiers, is unsuitable for cryogenic operation, as the carriers tend to freeze out below about 30 K. Gallium arsenide is a viable material for cryogenic semiconductor devices, but all commercial GaAs devices are designed for high-frequency operation, and therefore suffer from large 1/f noise in the band relevant to this experiment. Fortunately, researchers on the Gravity Probe B experiment have demonstrated that at least one legacy GaAs device, the NE41137 MESFET, is suitable for cryogenic operation at low frequency [71–73]. We have acquired several of these transistors, and the obvious next step is to build cryogenic amplifiers based on these devices for low-frequency noise measurements. A possible schematic for such an amplifier is shown in Fig. 4.12. With cryogenic amplifiers, it is possible to shorten the cabling to the first amplification stage by a factor of ~ 20, and thereby avoid much of the attenuation attendant to high-impedance signals. Even considering the relatively low gain available in a simple common-source amplifier, the input-referred voltage noise is extremely low at cryogenic temperatures, and therefore this could be a highly effective way to eliminate much of the unwanted interference seen in this system.

Vdd

1K

NE41137

50Ω

From Device

50Ω

50Ω

To RT amplifiers

5K

150
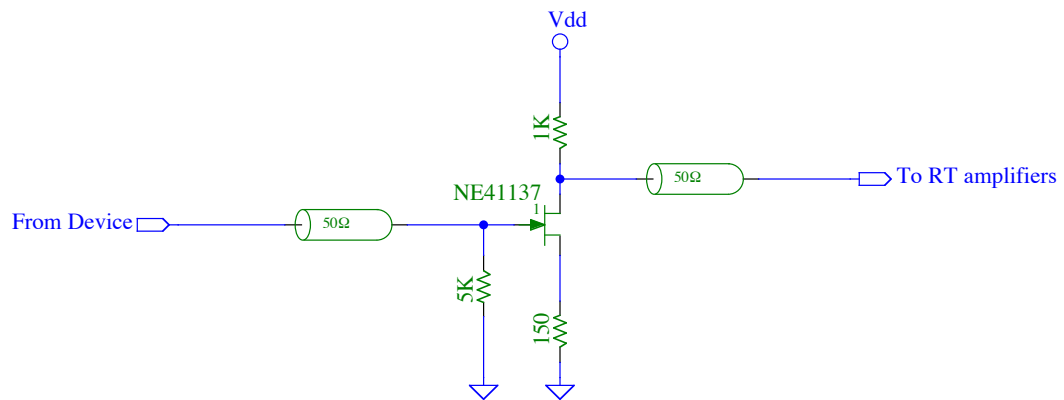
Figure 4.12 : Common-source cryogenic amplifier design utilizing the NE41137 MES-FET

Appendix A

Fabrication Recipes

In general, the patterning referenced herein is carried out by e-beam lithography (LEO S440 or JEOL JSM-6500 scanning electron microscope, in conjunction with the JC Nabity Nanometer Pattern Generation System [74]). Metallic films are deposited via e-beam evaporation in a system with a base pressure $\sim 10^{-7}$ mB (Edwards AUTO 400).

A.1 Nickel Nanocontacts for Magnetoresistance Measurements

Devices are fabricated on test-grade $p+$ silicon wafers with 200 nm thermal oxide (Montco Silicon). Wafer pieces are cleaned with acetone and rinsed with isopropanol, followed by O_2 plasma to remove organic residues. A film of poly(methyl methacrylate) with an average molecular weight of 950 kDa (PMMA-950) is then deposited from a 4% solution in chlorobenzene by spin coating at 3000 RPM for 40 s. The wafers are baked on a hot plate at 165 C for 1 hour. Following this bake, the nickel structures are patterned by SEM and developed with a mixture consisting of 1 part methyl isobutyl ketone (MIBK) and 3 parts isopropanol for 20 s, followed by a rinse in pure isopropanol and drying with clean nitrogen. The wafers are exposed to UV irradiation and ozone for 5 minutes to clean the exposed silicon surface. A 20 nm

thick Ni film is deposited by e-beam evaporation at a rate of 2 Å/s, and the remaining resist is lifted off with an acetone wash followed by an isopropanol rinse. The wafers are then cleaned with an Ar plasma to remove polymer residues from the surface.

A second film of PMMA with an average molecular weight of 495 kDa (PMMA-495) is then deposited from a 4% solution in anisole by spin coating at 3000 RPM for 40 s. This is followed by a 1-hour bake at 165 C in a reducing environment consisting of 10% hydrogen and 90% helium. Gold contact pads are then defined by SEM and developed for 40 s in a 1:3 mixture of MIBK and isopropanol, rinsed with pure isopropanol, and dried with clean nitrogen. The Ni surfaces are cleaned in a high-vacuum environment by sputtering with 500-eV Ar ions at a current of 10 mA for 60 s to facilitate good electrical contact to the leads. Leads are formed by evaporation of 1 nm Ti at 1 Å/s, followed by 30 nm Au at 2 Å/s. Lift-off of the remaining resist proceeds as before with acetone followed by an isopropanol rinse, drying with clean N_2, and Ar plasma.

A.2 Single-molecule Transistors for Transport and Noise Measurements

As above, devices are fabricated on test-grade $p+$ silicon wafers with 200 nm thermal oxide. Wafer pieces are cleaned with acetone, rinsed with isopropanol, and dried with clean dry N_2, followed by O_2 plasma cleaning to remove organic residues. PMMA-495 is deposited from a 4% solution in anisole, spun at 3000 RPM for 40 s to form a

thin layer, and baked at 165 C for 1 hour. The wafers are then patterned by SEM, developed for 20 s with a 1:4 mixture of MIBK and isopropanol, rinsed in isopropanol, and dried with clean N_2 gas. Wafers are exposed to UV irradiation and ozone for 5 minutes to clean the exposed silicon surface. 1 nm of Ti is deposited by e-beam evaporation at 1 Å/s, followed by 15 nm of Au at 2 Å/s. The wafers are washed in acetone to lift off the resist and undesired metal, rinsed in isopropanol, and dried with N_2 gas, followed by O_2 plasma to remove any resist residue. This may be followed by deposition of a self-assembled monolayer of molecules.

A.2.1 Alkanethiol Assembly

Alkanethiols used in control experiments include octanethiol ($C_8H_{17}SH$), decanethiol ($C_{10}H_{21}SH$) and dodecanethiol ($C_{12}H_{25}SH$). The self-assembly process is substantially the same for each of these molecules. A 1 mM solution of alkanethiol is prepared in ethanol. Clean, patterned, metallized chips are added to the solution, and self-assembly is carried out in a closed container in the dark for 48 hours. Samples are then rinsed well with isopropanol, dried with nitrogen, and measured in a vacuum cryostat.

A.2.2 BPDN Assembly

A monolayer film of Bipyridyl-dinitro oligo(phenylene ethynylene) dithiol (BPDN-DT) is assembled onto the gold surface as follows: A 0.2 mM solution of acetate-protected BPDN-DT is prepared in a 1:1 mixture of THF and ethanol. Dry nitrogen

gas is bubbled through this solution for 20 minutes to displace dissolved oxygen. Approximately 10 μL of ammonium hydroxide is added to deprotect the thiol moieties [55], and self-assembly is carried out in a closed container in the dark for 48 hours. Samples are then rinsed well with isopropanol, dried with nitrogen, and measured in a vacuum cryostat.

A.2.3   Transition Metal Complex Assembly

A 0.2 mM solution of transition metal complex [75] is prepared in nitrogen-purged THF. Self-assembly is carried out in a closed container in the dark for 48 hours. Samples are then rinsed well with isopropanol, dried with nitrogen, and measured in a vacuum cryostat.

Appendix B

Usage Guide for the attoCPSx4 Cryogenic Probe Station

B.1 Preface and Precautions

The attoCPSx4 cryogenic probe station is a versatile instrument, capable of making electronic measurements at temperatures as low as 1.4 K and magnetic fields up to 12 T. The heart of the attocube system is the four stacks of piezoelectric nanopositioners located around the sample stage. Each stack bears an electrical probe with signal and ground connections, and can address a sample space approx. 5 mm square. In the course of operations on this system, it is often necessary to handle parts of the instrument near the positioner stacks. *Exercise extreme caution when handling the stacks* – while the piezoelectric actuators can handle significant axial forces, any significant transverse force can crack the crystals and destroy the positioners. This fragility is compounded by the fact that when a positioner is extended, there is a relatively long lever arm for any forces exerted transverse to the axis of motion.

When preparing to attach or detach the piezo stacks from the microscope stick, the stick can be connected to its stand and placed upright on the counter. A stack can be held in place by its base while it is being screwed down (or unscrewed). When

unscrewing the circuit board material on top of a stack that holds the probe tips, the stack can be held by its topmost piece. Ideally, do not detach or re-attach the probe tips while the stacks are connected to the microscope stick.

This system requires liquid cryogens for low-temperature operation. As always, precautions for the safe handling of liquid cryogens should be observed during any transfer of liquid nitrogen or helium. Be sure that the room is well-ventilated, and wear appropriate PPE, including gloves and face shield.

The superconducting magnet in this system is basically a giant inductor. Remember Lenz's Law, and don't touch the magnet leads while the magnet is charged. In the event of a power failure, remember that the magnet is still on.

B.2   Loading and Unloading Samples

Samples are mounted on a copper stage which screws into the bottom of the microscope stick. Generally, it is necessary to detach the sample heater and temperature sensor leads before the stage can be removed. The current best practice for securing a sample is to mount it on a small piece of Kimwipe with a dab of Apiezon N grease. The Kimwipe electrically isolates the silicon from the stage, and the N grease provides enhanced thermal contact. After making sure that the chip is level, centered, and oriented properly, the stage can be put back into place and secured with two titanium screws.

B.3 Adjusting Optics and Inserting the Microscope Stick

After the chip is mounted, it is always a good idea to check its orientation through the microscope optics. A view of the sample is provided by a camera mounted atop the microscope stick, by way of a series of lenses in the tube. The lenses internal to the microscope stick are fixed and should not require adjustment. There is one lens between the top of the stick and the camera; this provides some level of zoom adjustment. Lowering the lens will magnify the image at the camera. After adjusting the zoom lens, the camera should be moved to restore focus. It may take several iterations to obtain a good image. Once you have acquired a satisfactory image, load the microscope stick into the stainless steel tube and *check it again.* You will never be sorry that you checked this — it takes a couple of minutes and can save you hours of warming, venting, and re-pumping the stick.

If a satisfactory image cannot be obtained once the sample is in the tube, there are a few possible reasons, with attendant remedies. Most likely, the sample is not lying completely flat on the stage. As silicon chips are highly polished, the strong tendency is towards specular reflection. If the chip is not facing directly up the tube, most of the light will be scattered to the sides of the tube instead of being collected by the lens system. The second most likely possibility is that the optics path is obstructed. Teflon tape is used to secure wires away from the optical path, but sometimes the tape starts to unwind and fall towards the center of the stick. If you suspect that this is the problem, remove the stick from the tube and verify that all of the tape is
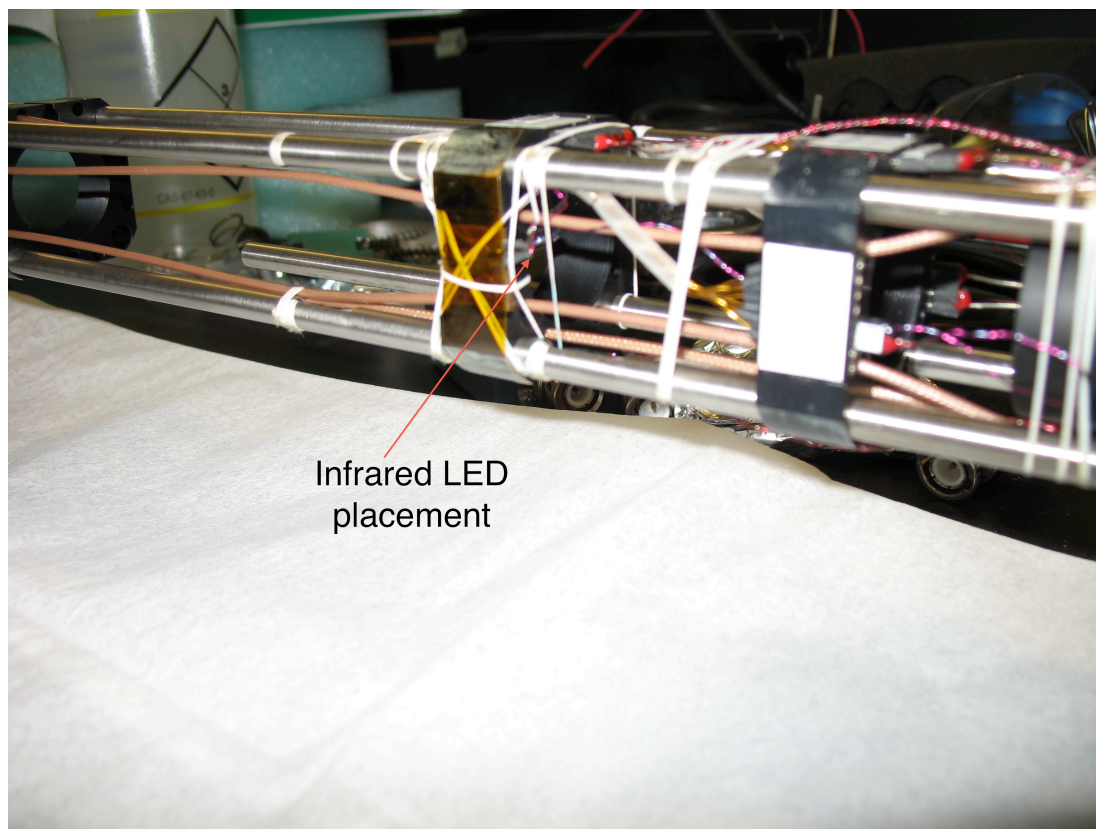
Figure B.1 : Photo showing proper placement of the infrared LED in the attocube probe station

in place. A third possibility is that the infrared LED, used to illuminate the sample, has been moved from its position or has failed to turn on. The placement of the LED is somewhat tricky, and may take some trial and error. Refer to Fig. B.1 for an approximate location.

Once a good optical path has been verified with the microscope stick in its stainless steel tube, it is time to evacuate the tube. Attach the turbo pump cart, make sure that all the valves are open, and start the pump. Once the pressure reads $\sim 2 \times 10^{-5}$

mB, close the solenoid valve and the valve at the top of the microscope stick. Purge the line from the helium cylinder with helium gas and attach it to the barbed fitting on the pump cart. Allow a small amount of helium gas in for thermal exchange – as a rule, I use about 6-7 inches of the tube filled with gas at 2 PSI. If you allow too much gas into the line, reopen the solenoid valve and pump the line back out. Be aware that this may take some time, as turbomolecular pumps are notoriously inefficient at removing helium gas. Once you have a satisfactory amount of gas in the line, keep the solenoid valve closed and open the valve at the top of the microscope stick to admit the gas. After the exchange gas has entered the microscope stick, close the valve at the top of the microscope stick again. You are now ready to insert the stick into the cryostat.

Close the line connecting the mechanical pump to the VTI space, connect a purged helium line to the barbed fitting atop the VTI, and flood the VTI with helium gas at about 2 PSI. The relief valve near the top of the VTI should pop to indicate that the VTI is at positive pressure. Remove the stainless cap from the compression fitting at the top of the VTI and slowly but steadily insert the stainless tube containing the microscope stick. Once the stick is fully inserted, cut off the helium supply and tighten the compression fitting well. Finally, open the valve to the mechanical pump to evacuate the VTI space and provide cooling power.
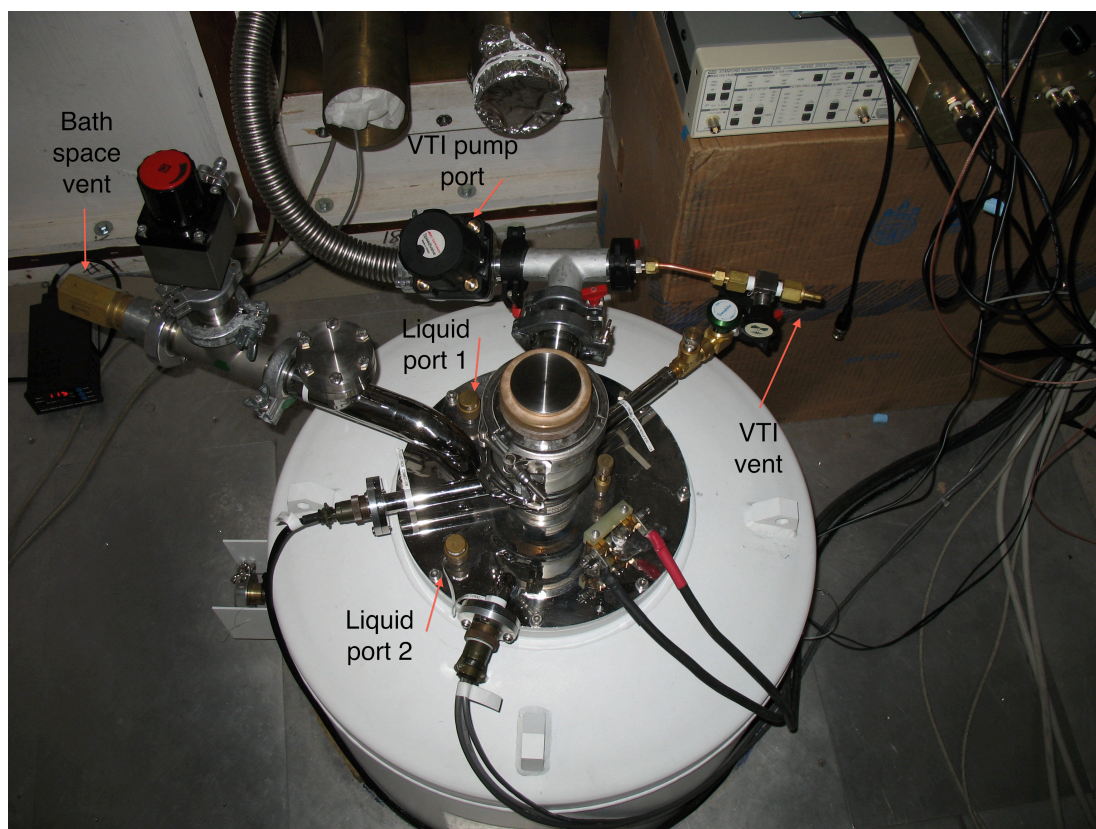
Figure B.2 : Photo of the top of the attocube dewar, with port numbers for reference

B.4   Cooling the sample and general operation

When starting with a warm cryostat the first step is to fill the bath space with liquid

nitrogen (LN). Fig. B.2 shows a view of the top of the attocube's dewar from above;

refer to this figure for port numbering.

Use a hose to connect the liquid port on a nitrogen dewar to the long, straight

stainless steel tube. Note that there are 4 notches in the bottom end of this tube.

The tube should be inserted into the cryostat through liquid port number 1 on the

cryostat. This port allows a tube to extend all the way to the bottom of the cryostat. Insert the tube until it hits the bottom of the cryostat and then lift it back up a few inches. This stainless steel tube can be used with a 3/4" to 5/8" brass adapter piece. When the tube is lifted up off the bottom of the cryostat, the compression seal of the adapter can be tightened to hold the tube in place. With the tube in place open the liquid valve on the nitrogen dewar. Make sure that the vent port to the cryostat bath space is uncovered.

It is vital to ensure that the needle valve does not become blocked or frozen. While the mechanical pump is pumping on the VTI space the needle valve is shut. During the filling process, periodically open the needle valve (this demonstrates that it is not frozen), and check that the reading on the pressure gauge goes up (this demonstrates that the passage is not blocked). The needle valve can be closed again after a few seconds. The critical times to check this are when the cryostat is being cooled and when the liquid level is below the needle valve. Once the liquid level is above the needle valve, it can be left shut for the time being.

The cryostat must be filled with LN at least until the magnetic is covered. Customarily, we fill with LN to a level about an inch above the top plate of the magnet; nitrogen is cheap, so it doesn't hurt to use more. To check the LN level during the filling process, remove the cap of liquid port number 2, which is adjacent to (and appears identical to) port number 1. This port has a path that only extends down to the magnet plate. Insert into this port the long black plastic rod until it hits the

top of the magnet plate. If the LN level is above the plate, one will be able to feel the plastic rod being agitated by the boiling liquid. Hold the tube in place for a few seconds before removing it and replacing the cap for port 2. Frost will quickly form on the plastic rod up to the top of the liquid level indicating the amount of LN in the cryostat. The filling process takes ~ 30 min.

When the LN level is sufficient, close the liquid valve on the nitrogen dewar. One can then either wait for the hose to unfreeze or use a heat gun to speed the process. When the hose has unfrozen, remove the stainless steel tube and replace the cap of liquid port number 1. The cryostat should be allowed to sit with the LN inside for at least one hour - overnight is better.

To remove the LN, open port 1 and re-insert the stainless steel tube. This time the tube should be *in contact with the bottom of the cryostat*. The compression fitting on the adapter for the stainless steel tube must be tight to ensure a good seal. The tube should still be connected to a hose which is attached to the liquid port of the nitrogen dewar. While the liquid port of the nitrogen dewar is still closed, fully open the vent valve of the nitrogen dewar. Wait until the pressure has reduced to atmosphere and the nitrogen gas is no longer venting at a high rate (takes about 10 minutes).

Attach a barbed hose fitting to the large vent port of the cryostat bath space. This may entail removing the large pressure relief valve. Attach a purged line of helium gas to this fitting in order to apply pressure to the LN in the bath space (pressure ~ 5 psi). Fully open the liquid port on the Nitrogen dewar. The LN in the cryostat

will be forced back into the nitrogen dewar. This may take around 30 minutes.

When the bath space is empty (or nearly empty) of LN an audible change will occur. As He gas is now flowing directly through the cryostat and into the dewar, the associated sound becomes distinctly louder. Wait for another minute or so to ensure that as much LN as possible is removed from the cryostat. During this time, the amount of He gas left in the cylinder should clearly drop.

At this point close the helium gas valve. Close the vent port and the liquid port on the nitrogen dewar. Slowly open the black valve connected via a Tee to the vent port of the cryostat bath space in order to relieve over pressure in the cryostat. When the hose has unfrozen remove the stainless steel tube and close the ports.

If the mechanical pump has been connected to the VTI, close the VTI valve and back fill the VTI space with helium gas until the small over pressure relief valve pops. Attach the mechanical pump to the bath space through the port normally used for the bath space pressure relief valve. Making sure all other ports are closed, turn on the mechanical pump and pump on the bath space for 45 - 60 minutes. Two things will indicate that no liquid nitrogen remains in the belly of the dewar. First, the pressure will start to fall dramatically. Second, the carbon resistor will start to warm slightly — this indicates that the resistor is no longer being cooled by evaporating nitrogen.

Once the liquid nitrogen is completely gone, attach a purged line of helium gas to the barbed fitting on the adjacent port to the bath space. Turn off the mechanical

pump and then slowly open the valve to allow helium gas into the bath space. An audible change occurs when the bath space is completely back filled with gas. To check the pressure, close the valve between the helium gas line and the bath space. Remove the helium gas line and with a thumb partially over the barbed fitting, slowly re-open the valve. If gas begins to blow out, you are ready to proceed. If your thumb is sucked against the port opening, continue filling the dewar with helium. When the bath space has been back filled with helium gas, re-connect the mechanical pump to the VTI space and start it pumping again. Leave the primary vent port to the bath space uncovered. Liquid helium (LHe) can now be added into the cryostat.

Place the liquid helium dewar halfway into the Faraday cage. Usually this means 2 wheels are inside the room and 2 wheels are outside. The port on the top of the dewar should be outside of the room to allow headroom for the rigid portion of the transfer stick. Attach a compression fitting with an adapter appropriate for the transfer tube to the top of the helium dewar. If the bath space of the cryostat is above liquid helium temperatures, make sure that the transfer tube extension piece is attached to the end of the transfer tube that will be inserted into the cryostat.

Open the side gas port valve on the helium dewar to relieve internal pressure. When the pressure has equilibrated, close this port valve and open the port on the top of the dewar. Begin slowly inserting the transfer tube. The end of the transfer tube that makes a right-angle is inserted into the storage dewar. The straight end is inserted into the cryostat. Close the over pressure port valve on the helium dewar.

When the tube is near the bottom of the dewar, bring the straight end of the tube inside the Faraday cage, then pull the helium dewar fully inside the cage as well. Bring the dewar close to the cryostat and make sure that the liquid port number 1 is uncovered. Wait a few minutes for the gas blowing out of the transfer tube to cool down and then insert this end into the cryostat. The tube should be inserted until it hits the bottom of the bath space.

If the cryostat is being re-filled with liquid helium while the bath space is already cold, it is very important to avoid inserting the transfer tube into the cryostat until liquid begins coming out (*i.e.* until the inside of the transfer tube has cooled to liquid helium temperature). This occurs when a jet of gas/liquid begins coming out of the end of the tube. If the tube is inserted while relatively warm gas is coming out, you will blow off a significant portion of the liquid remaining in the cryostat.

With the tube inserted and the bath space closer to liquid nitrogen temperatures, the cryostat must cool down before liquid will begin to accumulate inside. Inserting a warm transfer tube into a helium dewar will create a sufficient amount of pressure to begin this cooling. As this pressure dies down, in order to assist this process, a purged line of helium gas is connected to the gas port valve on the helium dewar with a pressure of ~ 1 psi. This port can be opened to allow additional pressure on the liquid in the dewar.

While the liquid helium filling process is beginning, this is another critical time to ensure that the needle valve does not become blocked or frozen. Just as before,

while the mechanical pump is pumping on the VTI space the needle valve is shut. While the bath space is cooling down toward 4 K, periodically open the needle valve for a few seconds and check that the reading on the pressure gauge goes up. If the pressure does not change at all, stop the filling process. The needle valve can be left shut for the remainder of the filling process when the helium liquid level is above 16" or so.

When the liquid helium reaches the desired level close the vent port on the dewar. Then close the valve on the helium gas cylinder and remove the helium gas hose from the gas port on the dewar. With the hose removed, open the gas port on the storage dewar to relieve pressure and stop the filling process. Remove the straight end of the transfer tube from the cryostat. Bring this end out of the Faraday cage, and then pull the storage dewar outside of the cage (or halfway out). Now the end of the transfer tube inside the dewar can be removed.

On the liquid helium dewar, close the gas port, close the top port, and open the overpressure relief port. On the cryostat, attach the large overpressure relief valve to the bath space port. Insert the microscope stick and vacuum tube, if they are not already inside, according to the steps described above.

With the microscope stick inserted, cooling your sample down can be accomplished by 2 methods. One can continue pumping on the VTI space with the mechanical pump and open the needle valve by a small amount. Alternatively, one can begin by closing the valve connected to the mechanical pump and then use a purged helium

gas line to over pressure the VTI space. The valve the helium gas can be closed again and the helium gas line should be removed. A length of hose a few feet long is then attached to the port where the helium gas line is normally connected. Now the needle valve should be opened by about 1 turn, and the valve on the port attached to the hose can be opened. Helium gas (boil-off) should be coming out of the end of this hose. Opening the needle valve more should increase the amount of gas coming out and closing the needle valve should reduce it. The amount of gas exiting the hose correlates to the rate at which the microscope stick is cooled down. The faster the rate the more liquid helium is lost. When cooling over a period of 6-8 hours, the needle valve should be approximately one half of a turn open. Listen to the gas coming out of the hose. If it is sputtering, then the needle valve can be opened more. This process will bring the VTI space and the sample temperature down to about 4.2 K.

B.5   Operation below 4.2 K

At atmospheric pressure, liquid helium boils at 4.2 K. The VTI, however, is capable of reaching temperatures as low as 1.4-1.5 K under the right conditions. The boiling point of helium decreases as the pressure above the helium is lowered. The simplest way to achieve a low VTI temperature, then, is to run the needle valve wide open (1-1.5 turns) until some amount of liquid accumulates in the annular space between the VTI inside wall and the stainless tube enclosing the sample space. Closing the needle

valve will cut off the supply of liquid from the main dewar, causing the pressure in the annulus to drop and lowering the boiling point of the liquid inside. This method achieves the lowest temperatures, but the liquid helium inside the annulus must be replaced from time to time — you can only run for $\sim$ 30 minutes below 4.2 K.

In order to run for long periods of time at temperatures below 4.2 K, some fine tuning of the gas flow is required. Starting with the system near 4.2 K, turn off all heaters and open the needle valve a full turn for approximately 5 minutes. This will allow some liquid to enter the annulus. Next, close the needle valve completely. The temperature should drop to about 1.5 K. Monitor the temperature for a few minutes until it starts to increase. When it does, open the needle valve slightly — between 1/4 and 1/3 turn should be sufficient to maintain the VTI temperature below 1.7 K for an indefinite period of time. It's a good idea to check the relation between valve position and VTI temperature from time to time. *Ceteris paribus*, it is best to run the VTI with the needle valve as close to the closed position as possible. This will minimize helium consumption.

B.6   Removing the microscope stick

Close the needle valve if it has been open. Close the line connecting the mechanical pump to the VTI space, connect a purged helium line to the barbed fitting atop the VTI, and flood the VTI with helium gas at about 2 PSI, or until the relief valve near the top of the VTI pops. Unscrew the compression fitting and steadily lift the

stainless steel tube up and out. After securing the vacuum tube and microscope, replace the stainless cap to close the VTI space and tighten the compression fitting. If the cryostat is cold, close the valve allowing helium gas into the VTI and then reopen the valve to the mechanical pump.

If the VTI space is very cold, it may be difficult to remove the stainless steel tube from the cryostat. Often, the O-ring on the sliding seal will freeze to the walls of the tube, preventing further movement. One way to reduce the chances that this will occur is to partially warm the VTI before removing the stick. Set the VTI temperature to 100 K, and wait several minutes while the sample temperature equilibrates near that point. Once the VTI is reasonably warm, proceed as above — a steady rate of withdrawal is still important to prevent sticking.

B.7   Magnet Operation

When using the 12 T magnet, great care must be taken to ensure that the rate at which the field is ramp up or down does not exceed the specification written down on the first page of the magnet manual. Turning on the power for the magnet creates a rather large EMF, and so if the magnet is to be used, it is recommended that the power be turned on before sample measurements begin. While the magnet is in use make sure that you do not bump the cryostat. In the case of a quench, open the Faraday cage door and open the door to the room. If possible, take off the pressure relief valve for the bath space. The magnet can only be operated when the liquid

helium level is above the top of the magnet. As a precaution, we only turn the field on if the liquid level is above the magnet top plate, which is at around 16".

Appendix C

Low-noise voltage preamplifiers with extremely high input impedance

Voltage measurements on high-impedance devices, such as tunnel junctions and single-molecule transistors, present some interesting measurement challenges. In particular, it is essential that the amplifier present as high an impedance as possible to the device, and bias current and current noise must be kept to a minimum. While many commercial amplifier designs are optimized for low voltage noise, the input impedance and current noise performance often leave a lot to be desired. With this in mind, we have designed and constructed a matched pair of voltage preamplifiers using a JFET input stage specified to provide an input impedace > 1 TΩ. These amplifiers are designed to provide a high-impedance, low-noise measurement facility in the band used in our single molecule noise measurements — DC to 100 kHz.

C.1 Architecture

Figure C.1 shows the schematic for the voltage amplifiers described here. The front end of these amplifiers is a straightforward differential-input configuration employing the Linear Technologies LT1169, a commercial FET input op-amp. The LT1169 is specified to provide input-referred voltage noise of less than $8 \frac{\text{nV}}{\sqrt{\text{Hz}}}$, current noise

$\sim 1\frac{\text{fA}}{\sqrt{\text{Hz}}}$, and a differential impedance of $10^{13}\Omega$ [76]. A rotary switch is used to select a gain of 10, 20, 50, or 100 in this stage. An ac coupling circuit after the front end makes it possible for this amplifier to operate at maximum gain with dc biases as large as 100 mV, and at reduced gain with dc biases up to 1 V. Given that energy scales in single molecules are often of this order of magnitude, the ability to operate with high biases is an essential facility for certain electron transport measurements in single molecules. The placement of the ac coupling circuit after the input stage enables us to retain a very high input impedance without risking saturation due to the amplifier's input bias current. The output stage consists of a commercially-available instrumentation amplifier, the Texas Instruments INA128 [77], configured with a selectable gain of 10 or 100. Noise and input impedance are secondary concerns for the output stage: even a low-cost output amplifier will have a relatively small noise contribution when referred to the input of the front end, and the input stage provides a low-impedance output to drive the second stage. The output stage also provides the ability to null any dc offset from the first stage.

Trimming potentiometers allow us to tune the gain at each stage, in order to provide the best possible matching between amplifiers. This is important for the cross-correlated noise measurement described in Section 4.2. The cross-correlation can only suppress that portion of the noise which appears in only one channel or the other, and if the amplifier noise on one channel is significantly larger than that on the other, some of the amplifier noise will leak through to the measured spectrum.

84

Figure C.1 : Schematic for the high-impedance voltage amplifier

C.2 Performance

Input-referred voltage noise spectra for these amplifiers are shown in Figs. C.2 and C.3. As expected, the overall input-referred voltage noise for these amplifiers is slightly higher than that of the input stage, $\sim 12\frac{\text{nV}}{\sqrt{\text{Hz}}}$, with the *1/f* corner appearing at 30 Hz. The increased level of white noise reflects the Johnson noise in the gain-setting network. Gain and phase are shown as a function of frequency in Fig. C.4 and subsequent figures. Particularly at the lower gain settings, we retain nearly-constant gain and good phase characteristics through much of the band of interest.
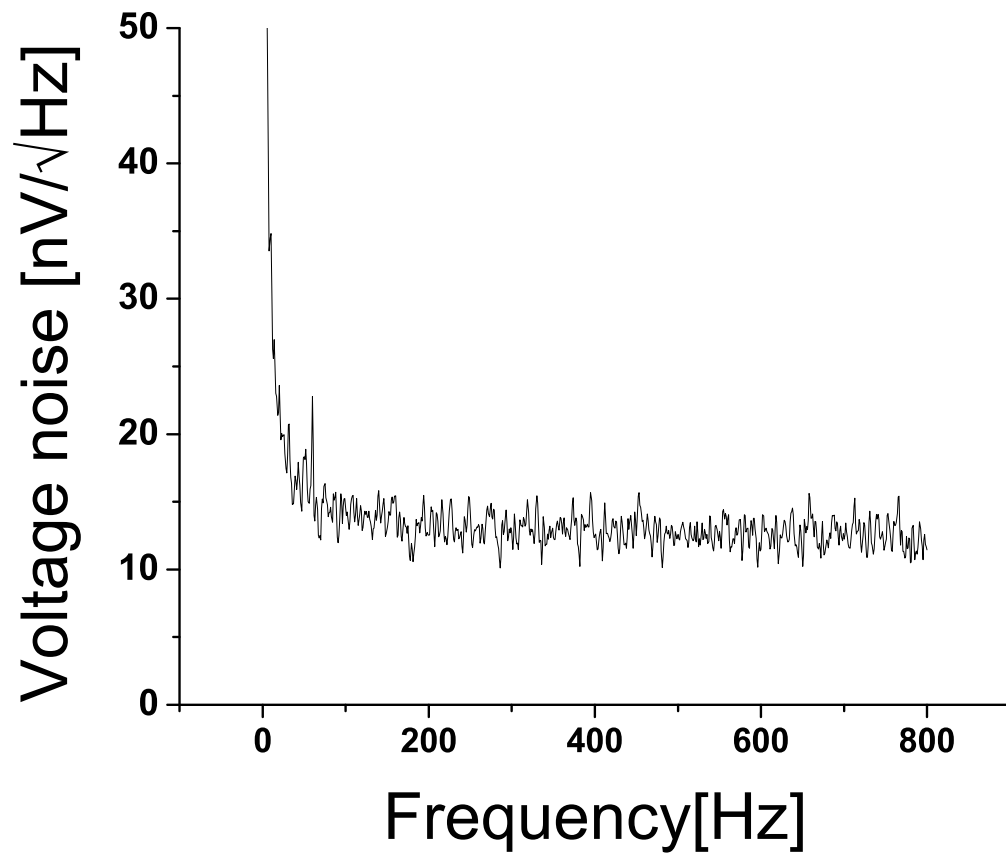
Figure C.2 : Input-referred voltage noise for the JFET-input amplifer with G = 100. This spectrum shows the corner for *1/f* noise at 30 Hz.
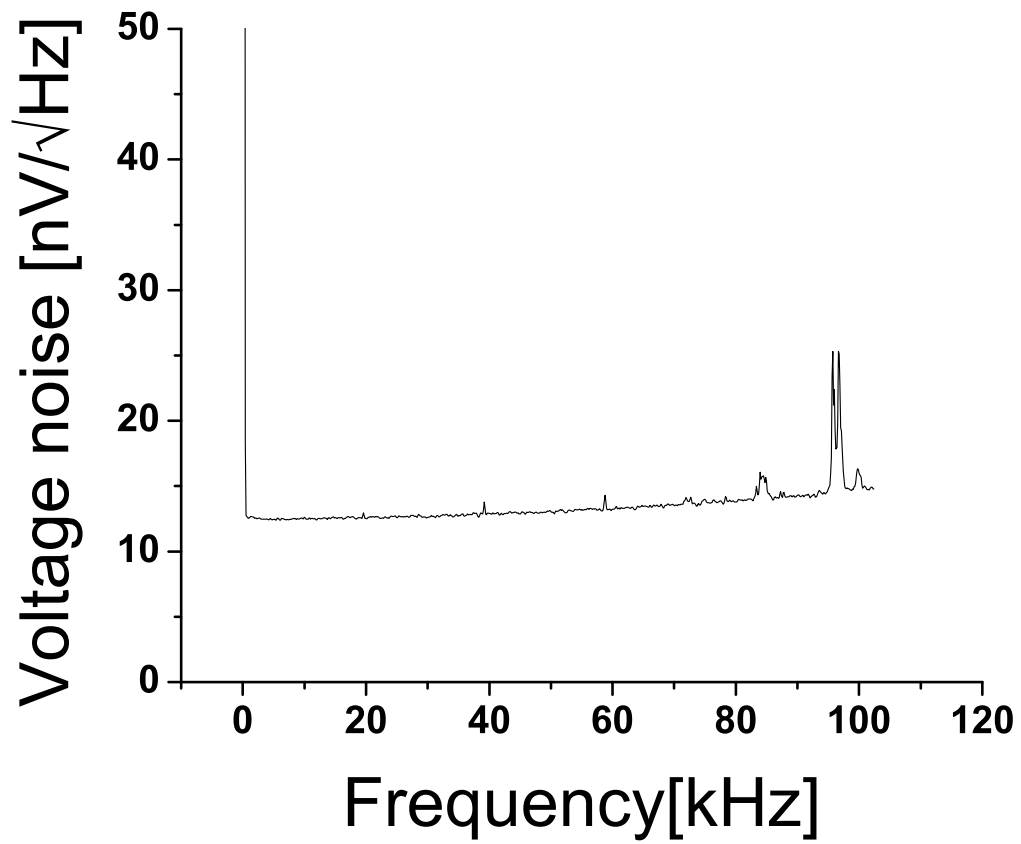
Figure C.3 : Input-referred voltage noise for the JFET-input amplifer with G = 100. This shows the overall noise spectrum from DC-100 kHz, verifying the expected figure $\sim 12\frac{\text{nV}}{\sqrt{\text{Hz}}}$

Figure C.4 : Gain and phase as a function of frequency for the JFET-input amplifier, measured via lock-in technique with a 100 μV excitation. Front-end gain is set at 10 and back-end gain is set at 10.

Figure C.5 : Gain and phase as a function of frequency for the JFET-input amplifier, measured via lock-in technique with a 100 μV excitation. Front-end gain is set at 10 and back-end gain is set at 100.
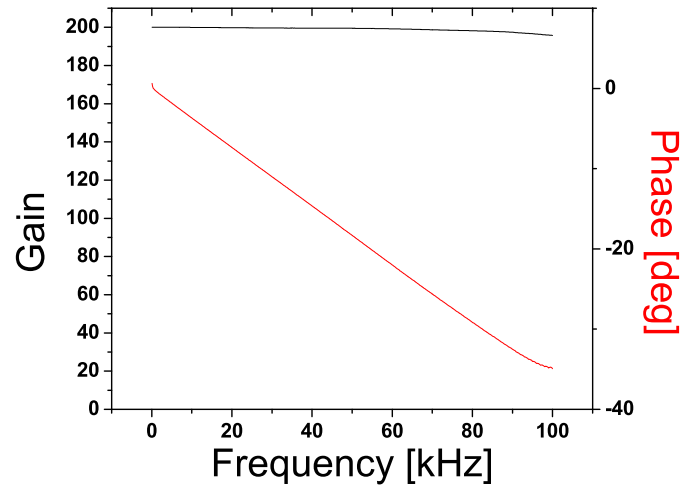
Figure C.6 : Gain and phase as a function of frequency for the JFET-input amplifier, measured via lock-in technique with a 100 μV excitation. Front-end gain is set at 20 and back-end gain is set at 10.
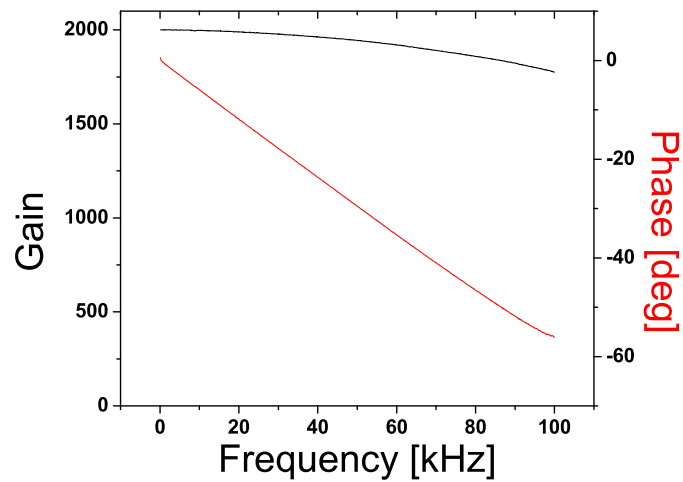
Figure C.7 : Gain and phase as a function of frequency for the JFET-input amplifier, measured via lock-in technique with a 100 μV excitation. Front-end gain is set at 20 and back-end gain is set at 100.
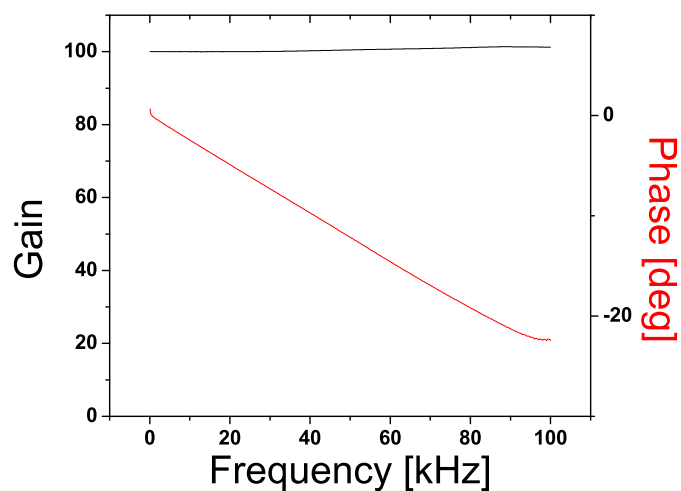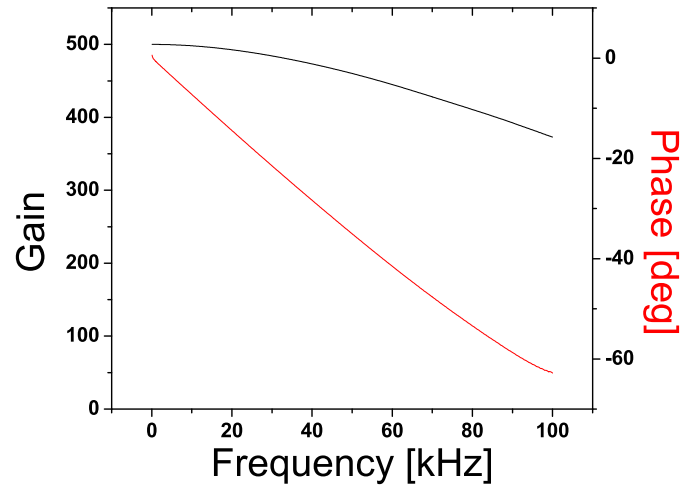
Figure C.8 : Gain and phase as a function of frequency for the JFET-input amplifier, measured via lock-in technique with a 100 μV excitation. Front-end gain is set at 50 and back-end gain is set at 10.
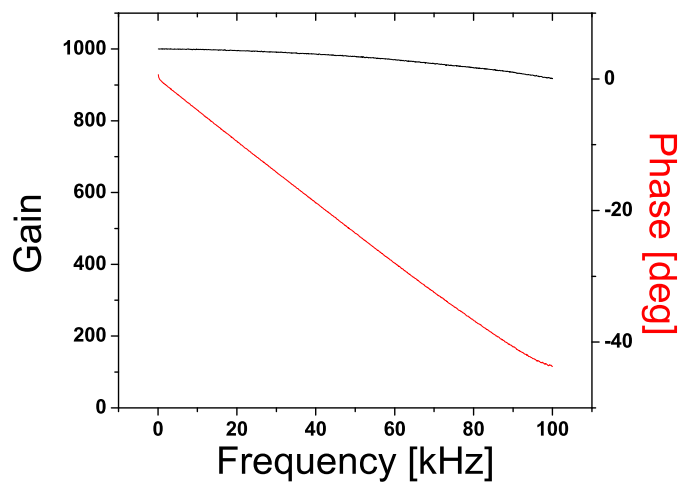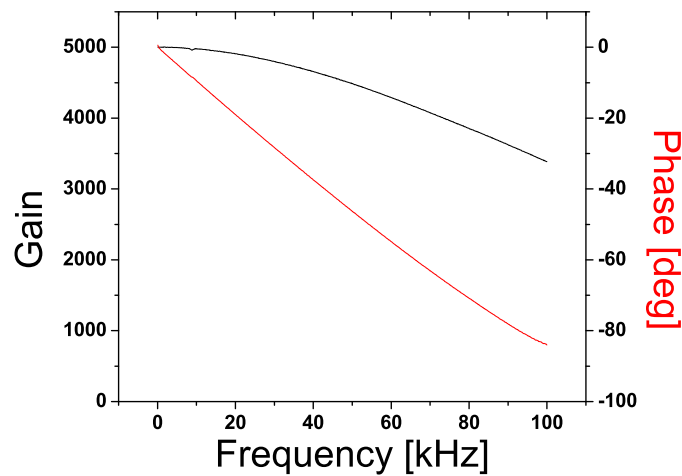

Figure C.9 : Gain and phase as a function of frequency for the JFET-input amplifier, measured via lock-in technique with a 100 μV excitation. Front-end gain is set at 50 and back-end gain is set at 100.
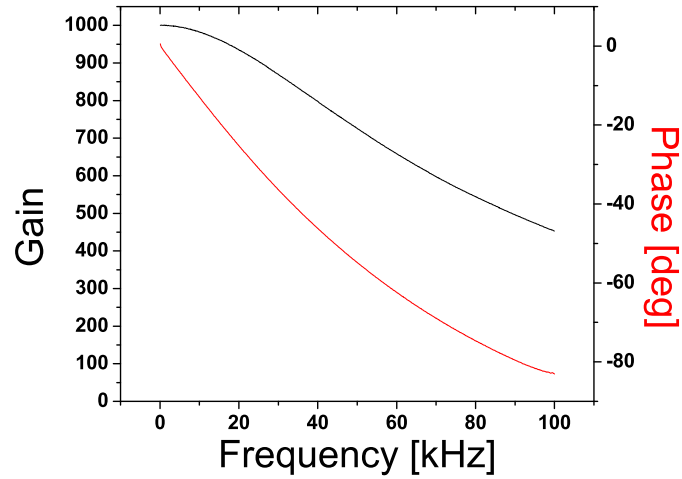
Figure C.10 : Gain and phase as a function of frequency for the JFET-input amplifier, measured via lock-in technique with a 100 μV excitation. Front-end gain is set at 100 and back-end gain is set at 10.
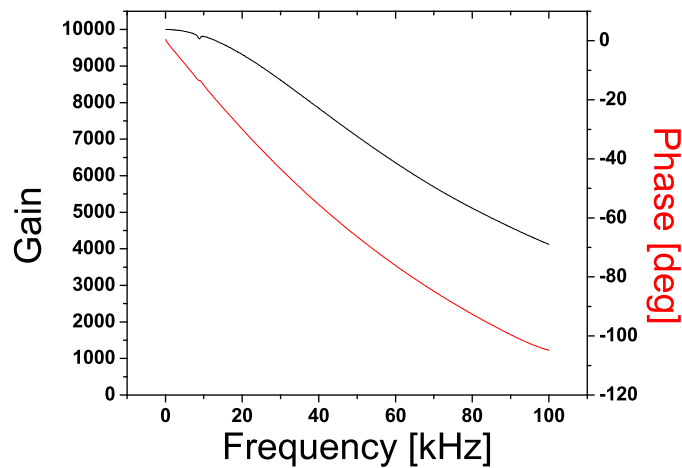
Figure C.11 : Gain and phase as a function of frequency for the JFET-input amplifier, measured via lock-in technique with a 100 μV excitation. Front-end gain is set at 100 and back-end gain is set at 100.

C.3   Parts list

Designator	Description
R1	100 Ω
R2	100 Ω
R3	470 Ω 0603
R4	1 kΩ 0603
R5	1 MΩ
R6	100 kΩ
R7	820 Ω 0603
R8	1 kΩ
R9	100 kΩ
R10	10 kΩ
R11	100 kΩ 0603
R12	10 kΩ 0603
R13	0.1 Ω 1206
R14	0.1 Ω 1206
C1	1 nF 1206
C2	47 uF
C3	1 uF 1206
C4	100 nF 1206
C5	100 nF 1206
D1	1N4001
D2	1N4001
D3	Schottky diode
D4	LED
D5	Schottky diode
Q1	ZXMN3A01F
Q2	ZXMN3A01F
Q3	2N7002
U1	DS2715

R15	499 Ω 1210
R16	50 Ω trimmer
R17	4.99 kΩ1210
R18	499 Ω1210
R19	200 Ω trimmer
R20	20 k Ω 1210
R21	300 Ω 1210
R22	100 Ω 1210
R23	160 kΩ 1210
R24	10 Ω trimmer
R25	750 Ω 1210
R26	47 Ω 1210
R27	10 MΩ 1210
R28	50 Ω trimmer
R29	160 kΩ 1210
R30	1 kΩ 1210
R31	1 kΩ 1210
R32	200 Ω trimmer
R33	3.9 kΩ 1210
R34	470 Ω 1210
R35	200 Ω trimmer
R36	100 kΩ 1210
R37	20 kΩ 1210
R38	1.24 kΩ 1210
R39	1.24 kΩ 1210
C6	100 nF 1210
C7	100 nF 1210
C8	100 nF 1210
C9	1 μF 1210
C10	100 nF 1210

C11	1 μF 1210
C12	100 nF 1210
C13	100 nF 1210
U2	LT1169
U3	INA128
U4	OP77
U5	REF200AU
U6	REF200AU
U7	REF200AU
U8	REF200AU
S1	SPDT switch
S2	DPDT switch
S3	1P4T rotary shorting switch
S4	SPDT switch
P1	2-Pin Header
P2	2-Pin Header
P3	2-Pin Header
P4	Right-angle BNC
P5	Right-angle BNC
P6	Right-angle BNC
P7	Right-angle BNC
P8	2-Pin Header
L1	47 uH

Bibliography

[1] L. Brus, "Quantum crystallites and nonlinear optics," *Applied Physics A Solids and Surfaces*, vol. 53, p. 465, Dec 1991.

[2] C. T. Yavuz, J. T. Mayo, W. W. Yu, A. Prakash, J. C. Falkner, S. Yean, L. Cong, H. J. Shipley, A. Kan, M. Tomson, D. Natelson, and V. L. Colvin, "Low-field magnetic separation of monodisperse Fe_3O_4 nanocrystals," *Science*, vol. 314, pp. 964–967, Jan 2006.

[3] Y. Taur, "CMOS design near the limit of scaling.," *IBM Journal of Research & Development*, vol. 46, no. 2/3, p. 213, 2002.

[4] W. Haensch, E. J. Nowak, R. H. Dennard, P. M. Solomon, A. Bryant, O. H. Dokumaci, A. Kumar, X. Wang, J. B. Johnson, and M. V. Fischetti, "Silicon CMOS devices beyond scaling.," *IBM Journal of Research & Development*, vol. 50, no. 4/5, pp. 339 – 361, 2006.

[5] M. A. Topinka, B. J. LeRoy, S. E. J. Shaw, E. J. Heller, R. M. Westervelt, K. D. Maranowski, and A. C. Gossard, "Imaging coherent electron flow from a quantum point contact," *Science*, vol. 289, p. 2323, Sep 2000.

[6] M. N. Baibich, J. M. Broto, A. Fert, F. N. van Dau, F. Petroff, P. Eti-

enne, G. Creuzet, A. Friederich, and J. Chazelas, "Giant magnetoresistance of (001)Fe/(001)Cr magnetic superlattices," *Physical Review Letters*, vol. 61, p. 2472, Nov 1988.

[7] T. McGuire and R. Potter, "Anisotropic magnetoresistance in ferromagnetic 3d alloys," *IEEE Transactions on Magnetics*, vol. 11, p. 1018, Jul 1975.

[8] H. D. Chopra and S. Z. Hua, "Ballistic magnetoresistance over 3000% in Ni nanocontacts at room temperature," *Physical Review B*, vol. 66, p. 20403, Jun 2002.

[9] W. Thomson, "On the electro-dynamic qualities of metals:–effects of magnetization on the electric conductivity of nickel and of iron.," *Proceedings of the Royal Society of London*, Jan 1856.

[10] J. Smit, "Magnetoresistance of ferromagnetic metals and alloys at low temperatures," *Physica*, vol. 17, p. 612, 1951.

[11] M. Julliere, "Tunneling between ferromagnetic films," *Phys. Lett. A*, Jan 1975.

[12] N. García, M. Muñoz, and Y.-W. Zhao, "Magnetoresistance in excess of 200% in ballistic Ni nanocontacts at room temperature and 100 Oe," *Physical Review Letters*, vol. 82, p. 2923, Apr 1999.

[13] S. Z. Hua and H. D. Chopra, "100,000 % ballistic magnetoresistance in stable Ni nanocontacts at room temperature," *Physical Review B*, vol. 67, p. 60401, Feb

2003.

[14] W. F. Egelhoff, L. Gan, H. Ettedgui, Y. Kadmon, C. J. Powell, P. J. Chen, A. J. Shapiro, R. D. McMichael, J. J. Mallett, T. P. Moffat, M. D. Stiles, and E. B. Svedberg, "Artifacts in ballistic magnetoresistance measurements (invited)," *Journal of Applied Physics*, vol. 95, p. 7554, Jun 2004.

[15] M. Viret, S. Berger, M. Gabureac, F. Ott, D. Olligs, I. Petej, J. F. Gregg, C. Fermon, G. Francinet, and G. L. Goff, "Magnetoresistance through a single nickel atom," *Physical Review B*, vol. 66, p. 220401, Dec 2002.

[16] C.-S. Yang, C. Zhang, J. Redepenning, and B. Doudin, "In situ magnetoresistance of Ni nanocontacts," *Applied Physics Letters*, vol. 84, p. 2865, Apr 2004.

[17] O. Ozatay, P. Chalsani, N. C. Emley, I. N. Krivorotov, and R. A. Buhrman, "Magnetoresistance and magnetostriction effects in ballistic ferromagnetic nanoconstrictions," *Journal of Applied Physics*, vol. 95, p. 7315, Jun 2004.

[18] M. I. Montero, R. K. Dumas, G. Liu, M. Viret, O. M. Stoll, W. A. Macedo, and I. K. Schuller, "Magnetoresistance of mechanically stable Co nanoconstrictions," *Physical Review B*, vol. 70, p. 184418, Nov 2004.

[19] F. J. Jedema, A. T. Filip, and B. J. van Wees, "Electrical spin injection and accumulation at room temperature in an all-metal mesoscopic spin valve," *Nature*, vol. 410, pp. 345–8, Mar 2001.

[20] A. N. Pasupathy, R. C. Bialczak, J. Martinek, J. E. Grose, L. A. K. Donev, P. L. McEuen, and D. C. Ralph, "The Kondo effect in the presence of ferromagnetism," *Science*, vol. 306, p. 86, Oct 2004.

[21] H. Park, A. K. L. Lim, A. P. Alivisatos, J. Park, and P. L. McEuen, "Fabrication of metallic electrodes with nanometer separation by electromigration," *Applied Physics Letters*, vol. 75, p. 301, Jul 1999.

[22] D. R. Strachan, D. E. Smith, D. E. Johnston, T.-H. Park, M. J. Therien, D. A. Bonnell, and A. T. Johnson, "Controlled fabrication of nanogaps in ambient environment for molecular electronics," *Applied Physics Letters*, vol. 86, p. 3109, Jan 2005.

[23] J. Velev, R. F. Sabirianov, S. S. Jaswal, and E. Y. Tsymbal, "Ballistic anisotropic magnetoresistance," *Physical Review Letters*, vol. 94, p. 127203, Mar 2005.

[24] M. Gabureac, M. Viret, F. Ott, and C. Fermon, "Magnetoresistance in nanocontacts induced by magnetostrictive effects," *Physical Review B*, vol. 69, p. 100401, Mar 2004.

[25] D. Jacob, J. Fernández-Rossier, and J. J. Palacios, "Magnetic and orbital blocking in Ni nanocontacts," *Physical Review B*, vol. 71, p. 220403, Jun 2005.

[26] E. Y. Tsymbal, A. Sokolov, I. F. Sabirianov, and B. Doudin, "Resonant inversion of tunneling magnetoresistance," *Physical Review Letters*, vol. 90, p. 186602, May 2003.

[27] T.-S. Kim, "Inverse tunneling magnetoresistance in nanoscale magnetic tunnel junctions," *Physical Review B*, vol. 72, p. 24401, Jul 2005.

[28] K. I. Bolotin, F. Kuemmeth, A. N. Pasupathy, and D. C. Ralph, "From ballistic transport to tunneling in electromigrated ferromagnetic breakjunctions," *Nano Letters*, vol. 6, pp. 123–7, Jan 2006.

[29] A. M. Moore, A. A. Dameron, B. A. Mantooth, R. K. Smith, D. J. Fuchs, J. W. Ciszek, F. Maya, Y. Yao, J. M. Tour, and P. S. Weiss, "Molecular engineering and measurements to test hypothesized mechanisms in single molecule conductance switching," *J Am Chem Soc*, vol. 128, pp. 1959–67, Feb 2006.

[30] A. S. Blum, J. G. Kushmerick, D. P. Long, C. H. Patterson, J. C. Yang, J. C. Henderson, Y. Yao, J. M. Tour, R. Shashidhar, and B. R. Ratna, "Molecularly inherent voltage-controlled conductance switching," *Nature materials*, vol. 4, pp. 167–72, Feb 2005.

[31] J. G. Kushmerick, D. B. Holt, J. C. Yang, J. Naciri, M. H. Moore, and R. Shashidhar, "Metal-molecule contacts and charge transport across monomolecular layers: Measurement and theory," *Physical Review Letters*, vol. 89, p. 86802, Aug 2002.

[32] D. P. Long, C. H. Patterson, M. H. Moore, D. S. Seferos, G. C. Bazan, and J. G. Kushmerick, "Magnetic directed assembly of molecular junctions," *Applied Physics Letters*, vol. 86, p. 3105, Apr 2005.

[33] J. M. Seminario, A. G. Zacarias, and P. A. Derosa, "Analysis of a dinitro-based molecular device," *Journal of Chemical Physics*, vol. 116, p. 1671, Jan 2002.

[34] M. Galperin, M. A. Ratner, and A. Nitzan, "Hysteresis, switching, and negative differential resistance in molecular junctions: A polaron model," *Nano Letters*, vol. 5, p. 125, Jan 2005.

[35] M. Galperin, A. Nitzan, and M. A. Ratner, "The non-linear response of molecular junctions: the polaron model revisited," *Journal of Physics: Condensed Matter*, vol. 20, p. 4107, Sep 2008.

[36] A. S. Alexandrov, A. M. Bratkovsky, and R. S. Williams, "Bistable tunneling current through a molecular quantum dot," *Physical Review B*, vol. 67, p. 75301, Feb 2003.

[37] A. Mitra, I. Aleiner, and A. J. Millis, "Semiclassical analysis of the nonequilibrium local polaron," *Physical Review Letters*, vol. 94, p. 76404, Feb 2005.

[38] D. Mozyrsky, M. B. Hastings, and I. Martin, "Intermittent polaron dynamics: Born-oppenheimer approximation out of equilibrium," *Physical Review B*, vol. 73, p. 35104, Jan 2006.

[39] M. Galperin, M. A. Ratner, A. Nitzan, and A. Troisi, "Nuclear coupling and polarization in molecular transport junctions: Beyond tunneling to function," *Science*, vol. 319, p. 1056, Feb 2008.

[40] C. Collier, J. Jeppesen, Y. Luo, J. Perkins, E. Wong, J. Heath, and J. Stoddart, "Molecular-based electronically switchable tunnel junction devices," *J Am Chem Soc*, vol. 123, pp. 12632–12641, Jan 2001.

[41] M. di Ventra, S.-G. Kim, S. T. Pantelides, and N. D. Lang, "Temperature effects on the transport properties of molecules," *Physical Review Letters*, vol. 86, p. 288, Jan 2001.

[42] J. Cornil, Y. Karzazi, and J. Bredas, "Negative differential resistance in phenylene ethynylene oligomers," *J Am Chem Soc*, vol. 124, pp. 3516–3517, Jan 2002.

[43] G. K. Ramachandran, T. J. Hopson, A. M. Rawlett, L. A. Nagahara, A. Primak, and S. M. Lindsay, "A bond-fluctuation mechanism for stochastic switching in wired molecules," *Science*, vol. 300, p. 1413, May 2003.

[44] P. A. Lewis, C. E. Inman, F. Maya, J. M. Tour, J. E. Hutchison, and P. S. Weiss, "Molecular engineering of the polarity and interactions of molecular electronic switches," *J Am Chem Soc*, vol. 127, pp. 17421–6, Dec 2005.

[45] P. E. Kornilovitch and A. M. Bratkovsky, "Orientational dependence of current through molecular films," *Physical Review B (Condensed Matter and Materials Physics)*, vol. 64, p. 195413, Nov 2001.

[46] Z. J. Donhauser, B. A. Mantooth, K. F. Kelly, L. A. Bumm, J. D. Monnell, J. J. Stapleton, D. W. P. Jr, A. M. Rawlett, D. L. Allara, J. M. Tour, and

P. S. Weiss, "Conductance switching in single molecules through conformational changes," *Science*, vol. 292, pp. 2303–7, Jun 2001.

[47] H. van der Zant, Y. Kervennic, M. Poot, K. O'Neill, Z. de Groot, J. Thijssen, H. Heersche, N. Stuhr-Hansen, T. Bjornholm, D. Vanmaekelbergh, C. van Walree, and L. Jenneskens, "Molecular three-terminal devices: fabrication and measurements," *Faraday Discuss*, vol. 131, pp. 347–356, Jan 2006.

[48] D.-H. Chae, J. F. Berry, S. Jung, F. A. Cotton, C. A. Murillo, and Z. Yao, "Vibrational excitations in single trimetal-molecule transistors," *Nano Letters*, vol. 6, p. 165, Feb 2006.

[49] A. N. Pasupathy, J. Park, C. Chang, A. V. Soldatov, S. Lebedkin, R. C. Bialczak, J. E. Grose, L. A. K. Donev, J. P. Sethna, D. C. Ralph, and P. L. McEuen, "Vibration-assisted electron tunneling in c140transistors," *Nano Letters*, vol. 5, p. 203, Feb 2005.

[50] L. H. Yu and D. Natelson, "The Kondo effect in C_{60} single-molecule transistors," *Nano Letters*, vol. 4, p. 79, Jan 2004.

[51] H. Park, J. Park, A. Lim, E. Anderson, A. Alivisatos, and P. McEuen, "Nanomechanical oscillations in a single-C_{60} transistor," *Nature*, vol. 407, pp. 57–60, Sep 2000.

[52] L. H. Yu, Z. K. Keane, J. W. Ciszek, L. Cheng, M. P. Stewart, J. M. Tour,

and D. Natelson, "Inelastic electron tunneling via molecular vibrations in single-molecule transistors," *Physical Review Letters*, vol. 93, p. 266802, Dec 2004.

[53] L. H. Yu and D. Natelson, "Transport in single-molecule transistors: Kondo physics and negative differential resistance," *Nanotechnology*, vol. 15, p. 517, Oct 2004.

[54] A. Flatt, S. Dirk, J. Henderson, D. Shen, J. Su, M. Reed, and J. Tour, "Synthesis and testing of new end-functionalized oligomers for molecular electronics," *Tetrahedron*, vol. 59, pp. 8555–8570, Jan 2003.

[55] L. Cai, Y. Yao, J. Yang, D. Price, and J. Tour, "Chemical and potential-assisted assembly of thiolacetyl-terminated oligo(phenylene ethynylene)s on gold surfaces," *Chem Mater*, vol. 14, pp. 2905–2909, Jan 2002.

[56] L. H. Yu, Z. K. Keane, J. W. Ciszek, L. Cheng, J. M. Tour, T. Baruah, M. R. Pederson, and D. Natelson, "Kondo resonances and anomalous gate dependence in the electrical conductivity of single-molecule transistors," *Physical Review Letters*, vol. 95, p. 256803, Dec 2005.

[57] A. V. Danilov, S. E. Kubatkin, S. G. Kafanov, K. Flensberg, and T. Bjørnholm, "Electron transfer dynamics of bistable single-molecule junctions," *Nano Letters*, vol. 6, p. 2184, Oct 2006.

[58] J. He, Q. Fu, S. Lindsay, J. W. Ciszek, and J. M. Tour, "Electrochemical origin of

voltage-controlled molecular conductance switching," *J Am Chem Soc*, vol. 128, pp. 14828–35, Nov 2006.

[59] M. Galperin, A. Nitzan, and M. A. Ratner, "Reply to comment by alexandrov and bratkovsky [cond-mat/0603467, cond-mat/0606366]," *arXiv*, vol. cond-mat.mtrl-sci, Jan 2006.

[60] A. B. A. Alexandrov, "Comment on 'hysteresis, switching, and negative differential resistance in molecular junctions: a polaron model', by m. galperin, m.a. ratner, and a. nitzan, nano lett. 5, 125 (2005),"

[61] M. Marsella, R. Reid, S. Estassi, and L. Wang, "Tetra[2,3-thienylene]: A building block for single-molecule electromechanical actuators," *J Am Chem Soc*, vol. 124, pp. 12507–12510, Jan 2002.

[62] J. B. Johnson, "Thermal agitation of electricity in conductors," *Physical Review*, vol. 32, p. 97, Jul 1928.

[63] H. Nyquist, "Thermal agitation of electric charge in conductors," *Physical Review*, vol. 32, p. 110, Jul 1928.

[64] D. C. Glattli, "Quantum shot noise of conductors and general noise measurement methods," Jan 2009.

[65] Y. M. Blanter and M. Büttiker, "Shot noise in mesoscopic conductors," *Physics Reports*, vol. 336, p. 1, Sep 2000.

[66] A. O. Gogolin and A. Komnik, "Full counting statistics for the Kondo dot in the unitary limit," *Physical Review Letters*, vol. 97, p. 16602, Jul 2006.

[67] E. Sela, Y. Oreg, F. von Oppen, and J. Koch, "Fractional shot noise in the Kondo regime," *Physical Review Letters*, vol. 97, p. 86601, Aug 2006.

[68] C. Mora, X. Leyronas, and N. Regnault, "Current noise through a Kondo quantum dot in a SU(n) Fermi liquid state," *Physical Review Letters*, vol. 100, p. 036604, Jan 2008.

[69] J. Koch and F. von Oppen, "Franck-Condon blockade and giant Fano factors in transport through single molecules," *Physical Review Letters*, vol. 94, p. 206804, May 2005.

[70] L. Dicarlo, Y. Zhang, D. T. McClure, C. M. Marcus, L. N. Pfeiffer, and K. W. West, "System for measuring auto- and cross correlation of current noise at low temperatures," *Review of Scientific Instruments*, vol. 77, p. 3906, Jul 2006.

[71] D. Camin, G. Pessina, E. Previtali, and G. Ranucci, "Low-noise preamplifiers for 1 K operation using gallium arsenide MESFETs of very low 1/f noise," *Cryogenics*, vol. 29, pp. 857–862, Aug 1989.

[72] D. V. Camin, G. Pessina, and E. Previtali, "Front-end in GaAs," *Nuclear Instruments and Methods in Physics Research Section A*, vol. 315, p. 385, May 1992.

[73] D. V. Camin, "A 1 K front-end electronics for a cryogenic bolometric detector," *Nuclear Instruments and Methods in Physics Research Section A*, vol. 277, p. 204, Apr 1989.

[74] J. C. Nabity and M. N. Wybourne, "A versatile pattern generator for high-resolution electron-beam lithography," *Review of Scientific Instruments*, vol. 60, p. 27, Jan 1989.

[75] J. W. Ciszek, Z. K. Keane, L. Cheng, M. P. Stewart, L. H. Yu, D. Natelson, and J. M. Tour, "Neutral complexes of first row transition metals bearing unbound thiocyanates and their assembly on metallic surfaces," *J Am Chem Soc*, vol. 128, pp. 3179–89, Mar 2006.

[76] L. Technologies, "LT1169 datasheet," tech. rep., 1994.

[77] Burr-Brown, "INA128 datasheet," tech. rep., 1995.